https://doi.org/10.1016/j.engstruct.2023.115989

A physics-informed and data-enhanced tensile stress-strain model for UHPFRC

Wei-He Liu[1], Lu-Wen Zhang[2] and Jian-Guo Dai[1*]

[1]Department of Civil and Environmental Engineering, The Hong Kong Polytechnic University, Hong Kong, China

[2]Department of Engineering Mechanics, School of Naval Architecture, Ocean and Civil Engineering, Shanghai Jiao Tong University, Shanghai 200240, China

Abstract

Despite the rapid developments in fundamental investigations and engineering applications of ultra-high-performance fiber reinforced concrete (UHPFRC), there is still lacking of a reliable tensile stress—strain model for UHPFRC in design guidelines. A generalized tensile stress—strain model for UHPFRC was developed for the first time. Through properly identifying unified model parameters, widely acknowledged experimental results were successfully reproduced by using a one-dimensional finite element model (FEM). A rich database was generated and granted with physics by the FEM model. Physical-consistent strength, ultimate strain and stress—strain models of UHPFRC were proposed, trained by model-generated data, and enhanced by experimental data. The proposed strength model and ultimate strain model predicted extensive experimental results with reasonable accuracy, giving mean absolute percentage errors (MAPE) of 12% and 25.3%, respectively. The established stress—strain model also predicted satisfactorily the full-range stress—strain curves tested by different research groups. It was evidenced that higher mean matrix cracking strength leads to higher ultimate strengths, less cracks, higher crack widths of UHPFRC at the ultimate state. This was elaborated for the first time, as caused by the dual action of snubbing effects and multi-crack interactions.

Keywords: Ultra-high-performance fiber reinforced concrete; Generalized stress—strain model; One-dimensional FEM; Physics-informed data-enhanced; Snubbing effect; Multiple crack interactions.

∗Corresponding author.

E-mail address: jian-guo.dai@polyu.edu.hk (J.G. DAI)

1. Introduction

Ultra-high-performance fiber reinforced concrete (UHPFRC) (Naaman 2007), emerging as an innovative and promising construction material, exhibits an unusual compressive strength higher than 150 MPa, a tensile strength of 8 MPa, as well as a high deformation capacity with the ultimate strain more than 10 times that of pure cement paste (Wille et al. 2014). The distinct tensile ductility of UHPFRC is achieved through the ability to carry further load after first cracking, which is endowed by the addition of high amount of steel fibers (usually higher than 2%). Steel fibers not only transfer load across the microcracks through interfacial friction, but also control the crack widths in UHPFRC to within 10~50 μm, which further improves the composites permeability and makes the composites more durable. The superior compression, tension, durability and energy absorption properties of UHPFRC have made it very attractive for field applications under various environmental and loading conditions, e.g., footbridge (Adeline 1998), high way infrastructure (Graybeal 2011), precast concrete piles (Vande Voort et al. 2008), seismic retrofitting of bridge substructures (Massicotte and Boucher-Proulx 2010) and security and blast mitigations (Rebentrost and Wight 2009; Zhong et al. 2021).

Although the technologies on the basis of which the UHPFRC is produced have been well established since 1994 (Bache 1981; Larrard and Sedran 1994), it is still considered a challenge to characterize the tensile behavior of UHPFRC, including the tensile stress—strain behavior and cracking characteristics. The most straightforward way to determine the tensile properties of UHPFRC is through direct uniaxial tension tests (Bian et al. 2021; Huang et al. 2022; Kim et al. 2012; Lao et al. 2022; Mi et al. 2022; Pyo et al. 2016; Pyo et al. 2015; Ryu et al. 2013; Sujivorakul and Naaman 2003; Wille et al. 2014; Wille et al. 2011a; Wille et al. 2011b), which provide the tensile stress-strain curves and cracking characteristics directly without having to resort to any inverse analysis. However, the direct tension tests are hard to perform because the experimental setup is complicated which requires specific attention when gripping and aligning the specimen to the loading axis, or otherwise leads to inaccurate results (Wille et al. 2014). Recently, four-point bending tests were frequently conducted together with inverse analysis method to obtain the tensile stress—strain behavior of UHPFRC (López et al. 2016; Yang et al. 2021; Zhu et al. 2021), which are easy to perform. Nonetheless, only the constitutive behavior was concerned in these tests, and the tensile cracking characteristics were usually overlooked. While the experimental tests are effective ways in characterizing the tensile properties of the specific UHPFRC under investigations, and provide reliable guides on its practical applications, it is costly and labor-intensive to design UHPFRC through a test and trial approach rather than relying on rational design guidelines.

To the best of the authors' knowledge, currently there is still lacking of a generalized tensile stress—strain model which is valid for UHPFRC with different matrix compressive strengths, and reinforced by fibers of different lengths, diameters and volume fractions, towards a reliable design rule for UHPFRC. This has never been achieved either through purely experimental data-based analysis (design-oriented) or through rational mechanical analysis (analysis-oriented model) (Jiang and Teng 2007). The reason should be two-fold. Firstly, the database available for direct tension tests of UHPFRC is very limited in the literature, probably due to the difficulties in performing the tests. Besides, since it is hard to align the specimen to the loading axis, the tensile responses of UHPFRC tested by different researchers may be representative of different boundary conditions, i.e., even the limited data in the literature are quite noisy (Mezquida-Alcaraz et al. 2021). Therefore, it is rocky to develop a reliable stress—strain model for UHPFRC based on limited and noisy data. Particularly, Wille et al. (2014) conducted high-quality direct tension tests on UHPFRC reinforced by straight, twisted and hooked steel fibers, respectively, and performed a detailed regression analysis on all aspects of the tensile stress—strain behavior of UHPFRC, including the ultimate strength, ultimate strain, strain hardening modulus, unloading modulus, softening curves, energy absorptions, etc.

However, although they proposed general formulas for these quantities in terms of the fiber aspect ratio, fiber volume fraction and interfacial strength, most of these formulas degenerate to a function of fiber volume fraction only, through best fittings. This is a consequence of the limited experimental data involved in the derivations, which also limits the applicability of their model for more general design of UHPFRC.

Secondly, it is difficult to perform physics-based analysis to study the tensile cracking behavior of UHPFRC, which is intrinsically a highly nonlinear multiscale problem (Liu and Zhang 2019; Mi and Pan 2022). Specifically, the steel fibers, which are thousands of times smaller in dimension than the matrix material, interact with the matrix through nonlinear interfaces, and bridge varying numbers of microcracks which open and close repeatedly (Liu et al. 2020). Based upon simplified assumptions, a lot of one-dimensional micromechanics-based models for strain hardening cementitious composites (SHCC) or UHPFRC/HPFRC have been proposed (Abrishambaf et al. 2019; Aveston 1971; Kanda et al. 2000; Krstulovic-Opara and Malak 1997; Li et al. 2019; Lu and Leung 2016; Malak and Krstulovic-Opara 2019; Qu et al. 2020; Shah 1988; Tjiptobroto 1991; Tjiptobroto and Hansen 1991, 1993a, b; Zhou and Feng 2023), which relate the micromechanical parameters (e.g., fiber-matrix interfacial strength, fiber aspect ratio, matrix tensile strength) to the composites stress—strain behavior.

Some of these models (Abrishambaf et al. 2019; Kanda et al. 2000; Li et al. 2019; Lu and Leung 2016; Qu et al. 2020) were formulated on the basis of stress analysis, i.e., the strength profile of the cement matrix was compared with the applied stress in a step-by-step manner to determine when and where each new crack forms, which is limited to be at least a load transfer distance x_d away from any old cracks. The composites ultimate strength was assumed equal to the single-cracking bridging strength, and the crack width was determined by the bridging stress—crack opening (σ—δ) curve. Then the composites strain was calculated by the widths of all cracks. Although this method was shown to have reproduced stress—strain curves conforming with test results in a simple and efficient way , the derivation of the load transfer distance x_d , bridging stress—crack opening ($\sigma—\delta$) relationship, and thus the crack width were all based on single cracking analysis (Aveston and Kelly 1973; Stang and Shah 1986; Yang et al. 2008), with the multi-crack interactions being overlooked. Therefore, the applicability of these models should be susceptible in multiple cracking analysis (see Appendix A).

Others combined the conservation of energy principle and fracture mechanics approach to analyze the stress—strain response of SHCC (Aveston 1971; Krstulovic-Opara and Malak 1997; Malak and Krstulovic-Opara 2019; Tjiptobroto 1991; Tjiptobroto and Hansen 1991, 1993a, b). The conservation of energy principle (Aveston and Kelly 1973; Tjiptobroto and Hansen 1993a, b) was used to derive the elastic strain at the first peak (composites cracking strain) and the strain at the ultimate stress (Krstulovic-Opara and Malak 1997; Malak and Krstulovic-Opara 2019; Tjiptobroto 1991). Different energy terms were distinguished at the first cracking and subsequent multiple cracking process. For example, Tjiptobroto and Hansen (1993b) studied the tensile stress—strain response of short random fiber FRC by assuming that the external work which leads to the formation of the first crack is consumed by the matrix fracture energy, the strain energy released by the matrix upon first cracking and the strain energy stored in fibers induced by crack bridging; while between first cracking and the ultimate state, the matrix-related energy was replaced by the fiber debonding energy and interfacial frictional energy. Individually, the ultimate strength of SHCC was derived using a fracture mechanics approach (Aveston 1971; Krstulovic-Opara and Malak 1997; Malak and Krstulovic-Opara 2019; Stang and Shah 1986). In the derivations by Krstulovic-Opara and Malak (1997), they explicitly considered the number of cracks, but eventually obtained the same strength formula to that formulated by Stang and Shah (1986) on the basis of single cracking analysis.

In spite of the fact that the basic principles adopted by these models, i.e., the conservation of energy principle and fracture mechanics, are physically consistent and rational, when deriving the ultimate strain and ultimate strength, they have assumed that the fiber strain in the middle of adjacent cracks be equal to the matrix strain, implying perfect bonding and negligible fiber stress there. This holds true only when the crack spacing is larger than twice of the stress transfer length such that adjacent cracks do not disturb each other. Otherwise, a substantial level of fiber strain (much higher than matrix strain) and fiber stress can be developed in the middle of two adjacent cracks (Liu et al. 2022) due to multi-crack interactions (see also Appendix A). Besides, the ultimate strength of short random fiber reinforced cementitious composites under multiple cracking has been confirmed to be notably lower than that under single cracking, both experimentally (Naaman and Homrich 1989) and numerically (Liu et al. 2022). Although this phenomenon does not necessary occur in aligned continuous fiber composites due to the lack of snubbing effect (Krstulovic-Opara and Malak 1997), it is ubiquitous in short random fiber composites, which cannot be captured by these models, either, because they missed the multi-crack interactions. It is also worth noting that none of the existing micromechanics-based models has ever demonstrated its ability to predict the experimental data on tensile tests of SHCC/UHPFRC from many different research groups, which is a prerequisite for its wide applicability.

Now that simple yet reliable analytical models or micromechanics-based semi-analytical models are unavailable for tensile behavior of UHPFRC, finite element models can take over the role in the development of physics-informed constitutive models (Lu et al. 2005; Zhang et al. 2013) for UHPFRC, provided that physically-consistent constitutive laws and interactive mechanisms for fibers and matrix are installed (Fish et al. 2021; Zhang et al. 2022) to properly capture debonding, pullout and rupture of fibers and matrix cyclic cracking. Currently, the most realistic FEM model for UHPFRC is the explicit modeling method, where the kinematics and stresses of each discrete fiber is described independently from the cement matrix (Bitencourt et al. 2019; Carvalho et al. 2020; Tan and Martínez-Pañeda 2021; Zhang et al. 2018). The fibers were modeled as truss or beam elements, while the matrix cracking was described using a smeared crack model (Zhang et al. 2018), which may fail to capture the crack opening and the highly concentrated fiber stress at the discrete cracks. Another issue is that the fiber pullout, which is one of the dominating damage mechanisms in UHPFRC, was usually modeled by using an empirical exponential softening interface law. Therefore, the physics may be interpreted with unknown errors. Moreover, explicitly drawing meshes for discrete fibers and matrix material introduces enormous computational expenses, which is disadvantageous for generating a big database for analysis.

More recently, Liu et al. (2022) proposed a one-dimensional plastic-damage multiphase model to analyze the strain hardening behavior of UHPFRC under uniaxial tension. Instead of modeling each discrete fibers explicitly, they idealized the full set of fibers which have the same projected position on the loading axis and the same orientation as a fiber bundle, and depicted the fiber orientation using the projected length of fiber bundle on the loading axis. By putting fiber bundles layer by layer over the matrix phase with pre-inserted potential cracks, the realistic bridging characteristics with respect to either any crack, any material point or any fiber were successfully replicated. Physics-based constitutive laws for the matrix cracks and fiber-matrix interfaces were also proposed to capture the cyclic matrix cracking, fiber debonding, fiber pullout and fiber rupture, i.e., the major set of damage mechanisms in UHPFRC. It was shown that the model can predict the tensile stress-strain behavior and the cracking characteristics of UHPFRC (steel fiber), SHCC (PVA fiber) and UHPECC (PE fiber) which are highly consistent with tests.

The present study was aimed at developing a physics-informed, data enhanced stress—strain model for UHPFRC under uniaxial tension, by using the FEM model proposed by Liu et al. (2022) and the limited experimental data in the literature on the direct tension test of

UHPFRC. This work represents the first attempt to develop a unified tensile stress—strain model of UHPFRC for various matrix compressive strengths, fiber lengths, fiber diameters and fiber volume fractions. The manuscript was organized as follows. Section 2 presents the basic FEM model concept, governing equations and the mathematical evolution of snubbing effect. In Section 3, the experimental data from (Sujivorakul and Naaman 2003; Wille et al. 2014; Wille et al. 2011a) are used to further validate the FEM model and identify the unified model parameters to be used in subsequent analysis; In Section 4, extensive FEM simulations on uniaxial tensile tests of UHPFRC are conducted to generate the model-based data, which are then analyzed through regression to derive the strength model, ultimate strain model and stress—strain model for UHPFRC. The developed models are validated by experimental data in this section. Section 5 provides further insights into the underlying mechanisms informed by the stress—strain model developed in Section 4. The applicability and potential applications of the proposed model are discussed in Section 6. The conclusions are drawn in Section 7.

2. Finite Element Model

The basic model concept, governing equations and the snubbing effect for the one-dimensional model by Liu et al. (2022) were introduced in this section. Kinematic descriptions and constitutive laws, and implementation details of the finite element model were not presented here for brevity, interested readers are suggested to refer to (Liu et al. 2022).

2.1. Stacked fiber bundles model

Herein, the “fiber bundle” was defined as the full set of discrete fibers with the same longitudinal location and orientation. The model was constructed by stacking fiber bundles layer by layer over the whole matrix domain, where potential cracks $(\Gamma_1, \Gamma_2, ..., \Gamma_{14})$ were uniformly inserted a priori in a spacing which is equal to the element length l_e . Fig. 1(a) illustrated the stacking pattern of thirteen groups of fiber bundles $(G_1, G_2, ..., G_{13})$ of L_f . Each group G_I is composed of three individual fiber bundles G_I^1, G_I^2 and G_I^3 in the illustrative example, whose projection length L^1_{proj}, L^2_{proj} and L^3_{proj} on the X axis are l_e, $2\,l_e$ and $3\,l_e$, respectively. Accordingly, the inclination angle of any fiber bundle G_I^J was calculated by $\theta^J = \cos^{-1}(L^J_{proj}/L_f)$. Clearly, adopting a higher L_f/l_e ratio allows a higher degree of freedom in the choice of different discrete fiber orientations for approximating the realistic fiber orientation distribution of UHPFRC ($L_f/l_e = 3$ in Fig. 1(a)). Note that given L_f values, a higher L_f/l_e ratio can be achieved by adopting a smaller mesh size. Corresponding mesh convergence studies were conducted in (Liu et al. 2022) for mesh sizes of 2 mm, 1 mm, 1/2 mm and 1/3 mm. It was demonstrated that a mesh size of 1 mm is sufficient for discretizing fibers of length larger than 10 mm as well as for resolving the average crack spacing of different strain hardening fiber reinforced composites.

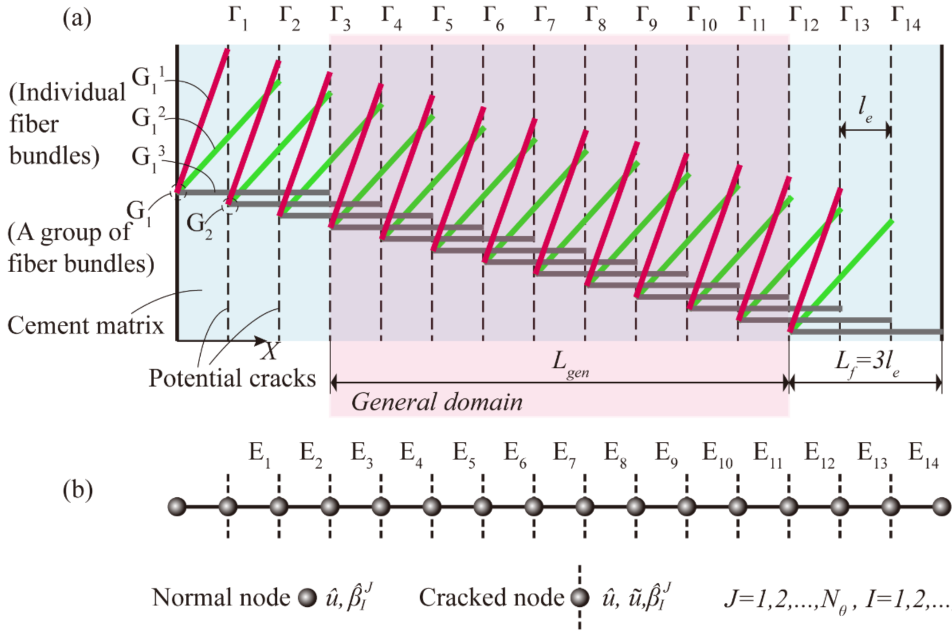

Fig. 1. (a) Stacked fiber bundles model; (b) Idealized 1-D model.

Inspired by the concept of gauge length in the direct tension test of UHPFRC where various mechanical quantities are measured, a general domain was defined in the stacked fiber bundles model (Fig. 1a), on which the focus of the analysis laid. In the general domain, the fiber bridging effect is uniformly accounted for. Specifically, each potential crack Γ_i in the general domain is equally crossed by fiber bundles inclined at different angles, with various embedment lengths. Besides, each material strip between two adjacent potential cracks is equally covered by fiber bundles inclined at different angles, with various distances between fiber bundles' left (or right) end and the material strip's left (or right) boundary. Moreover, fibers with the same orientation are crossed by the same number of potential cracks, while fibers inclined at higher angles are crossed by less potential cracks due to their smaller projected length on the loading axis (*X* axis).

2.2. The boundary value problem and snubbing effect

Following (Liu et al. 2022), the boundary value problem for a UHPFRC specimen under uniaxial tension was summarized as follows:

$$\left(\sigma_c\right)_{,X} = 0, \text{ in } \Omega \text{ , (1)}$$

$$\cos(\theta^J)\left(\sigma_I^J\right)_{,X} - \frac{4}{D_f}\tau_I^J = 0, \text{ in } \Omega_I^J \text{, (2)}$$

$$\sigma_c = \bar{\sigma}, \text{ on } \partial\Omega_{\bar{\sigma}} \text{, (3)}$$

$$u = \bar{u}, \text{ on } \partial\Omega_{\bar{u}} \text{, (4)}$$

$$\sigma_I^J = 0, \text{ on } \partial\Omega_I^J \text{, (5)}$$

$$v_m\sigma_m = v_m t_{i_\Gamma} + \sum_{J=1}^{N_\theta}\sum_{I=1}^{N_J} v_I^J \delta_{i_\Gamma} H_I^J \cos(\theta^J)(\left(\sigma_I^J\right)_{i_\Gamma} - \cos(\theta^J))\sigma_I^J, \text{ on } \Gamma_{i_\Gamma} \text{. (6)}$$

or equivalently

$$\sigma_c = v_m t_{i_\Gamma} + \sum_{J=1}^{N_\theta}\sum_{I=1}^{N_J} v_I^J \delta_{i_\Gamma} H_I^J \cos(\theta^J)\left(\sigma_I^J\right)_{i_\Gamma}, \text{ on } \Gamma_{i_\Gamma} \text{. (7)}$$

Eq. (1) is the macroscale balance equation which enforces that the composites bulk stress σ_c is constant over the UHPFRC specimen under uniaxial tension, with the composite bulk stress being defined as:

$$\sigma_c = v_m \sigma_m + \sum_{J=1}^{N_\theta} \sum_{I=1}^{N_J} v_I^J H_I^J \cos(\theta^J)^2 \sigma_I^J \text{ . (8)}$$

Eq. (2) interprets the fiber-matrix load transfer mechanism, Eq. (3) and (4) are the force and displacement boundary conditions, respectively, Eq. (5) imposes a zero-stress constraint at fiber ends, which is naturally satisfied.

In Eq. (6), the second term on the right-hand side is the so-called pulley force term (Lu and Leung 2016), where $\left(\sigma_I^J\right)_{i_\Gamma}$ is the bridging stress of fiber bundle G_I^J at the potential crack i_Γ. Note that in this paper σ_I^J refers to the fiber stress induced by normal interfacial friction only, whose evolution is governed by Eq. (2). The expression for $\left(\sigma_I^J\right)_{i_\Gamma}$ used to be defined as:

$$\left(\sigma_I^J\right)_{i_\Gamma} = e^{f\theta^J} \sigma_I^J \text{ , (9)}$$

where $e^{f\theta^J}$ is the amplification factor related to the snubbing effect, which is induced by the intense friction at the exist point of the fiber with respect to the crack surface, and f is the snubbing coefficient. However, Liu et al. (2022) claimed that Eq. (9) is only valid in single cracking analysis, because in multiple cracking, the fiber stress σ_I^J can develop to a high level at any potential crack i_Γ that has not been activated, i.e., inactive crack i_Γ, because interfacial debonding can be induced by the active cracks in the neighborhood of the inactive crack i_Γ (see Fig. A.1b). When the crack i_Γ becomes activated, the fiber bridging stress $\left(\sigma_I^J\right)_{i_\Gamma}$ should not unrealistically change from $\left(\sigma_I^J\right)^{inactive}$ to $e^{f\theta^J}\left(\sigma_I^J\right)^{inactive}$ instantaneously, where $\left(\sigma_I^J\right)^{inactive}$ denotes the fiber stress at the instant of crack activation. Instead, Liu et al. (2022) assumed the following evolution law for $\left(\sigma_I^J\right)_{i_\Gamma}$:

$$\dot{\left(\sigma_I^J\right)}_{i_\Gamma} = \begin{cases} \dot{\sigma}_I^J \delta_{i_\Gamma}, & \text{if } \Gamma_{i_\Gamma} \text{ is inactive} \\ e^{f\theta^J} \dot{\sigma}_I^J \delta_{i_\Gamma}, & \text{if } \Gamma_{i_\Gamma} \text{ is active} \end{cases} \text{ , (10)}$$

which means that the snubbing effect or the amplification factor $e^{f\theta^J}$ only prevails for the part of fiber stress $\left(\sigma_I^J\right)^{active}$ which develops after the crack i_Γ is activated, with

$$\sigma_I^J = \left(\sigma_I^J\right)^{inactive} + \left(\sigma_I^J\right)^{active}, \text{ at the active crack } i_\Gamma. \quad (11)$$

The application of this evolution law was proved to be successful in reproducing the stress—strain behavior and cracking characteristics of various strain hardening cementitious composites (Liu et al. 2022).

3. Parameter identification and model validation

The material parameters under investigated are the fiber length L_f, fiber diameter D_f, fiber volume fraction V_f, interfacial friction stress τ_0, mean matrix cracking stress σ_{mc} and interfacial stiffness k_i. Other parameters (Liu et al. 2022), including matrix Yong's Modulus E_m, fracture energy G_m, unloading parameter w^z; fiber Young's Modulus E_f, tensile strength σ_f^y, orientation distribution FOD, strength reduction coefficient f'; interface hardening parameter β_f, snubbing coefficient f, and fiber rupture parameter w_{ref} were unified by fitting the finite element model predictions with direct tension test results from (Sujivorakul and Naaman 2003; Wille et al. 2014; 2011a). The unified parameters are summarized in Table E.1, while Table E.2 summarizes corresponding specific parameters of the experimental database. The fiber orientation and matrix strength distributions were determined as described in Appendix C. Without loss of generality, all the simulations in this work were conducted with a mesh size of 1mm and gauge length of 76 mm. The mesh size objectivity has been demonstrated in (Liu et al. 2022), thus was not studied here.

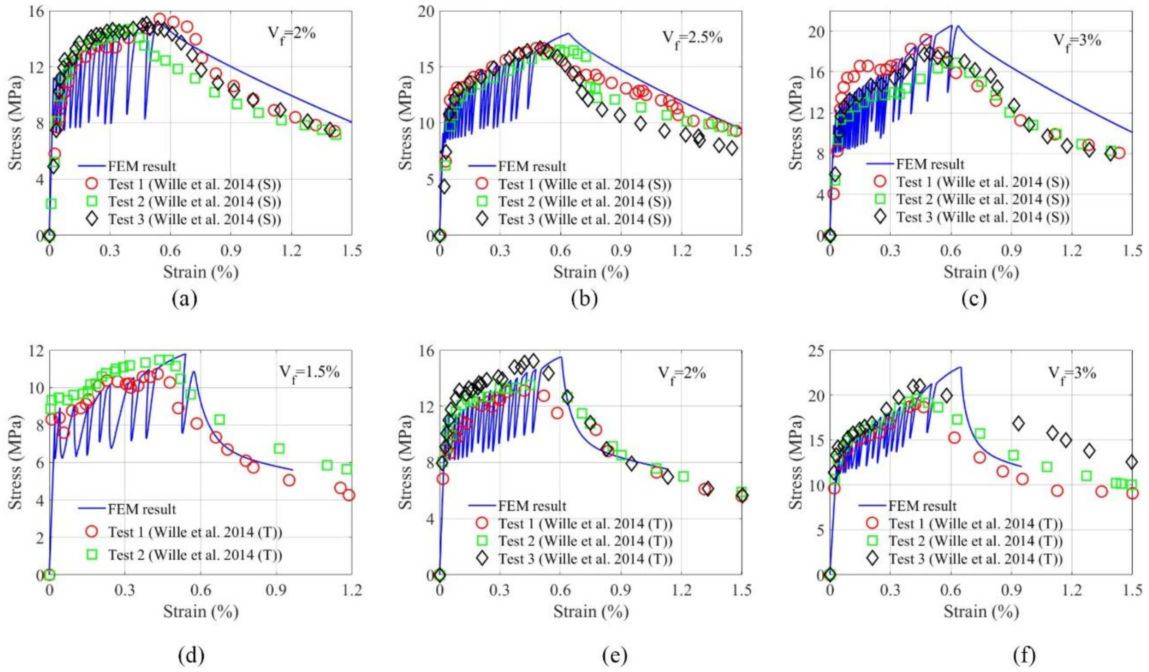

Fig. 2. Comparisons of the tensile stress—strain curves from FEM simulations and from experiments by Wille et al. (2014), for UHPFRC reinforced with (a) 2%, (b) 2.5% and (c) 3% of straight steel fibers, and (d) 1.5%, (e) 2% and (f) 3% of twisted steel fibers.

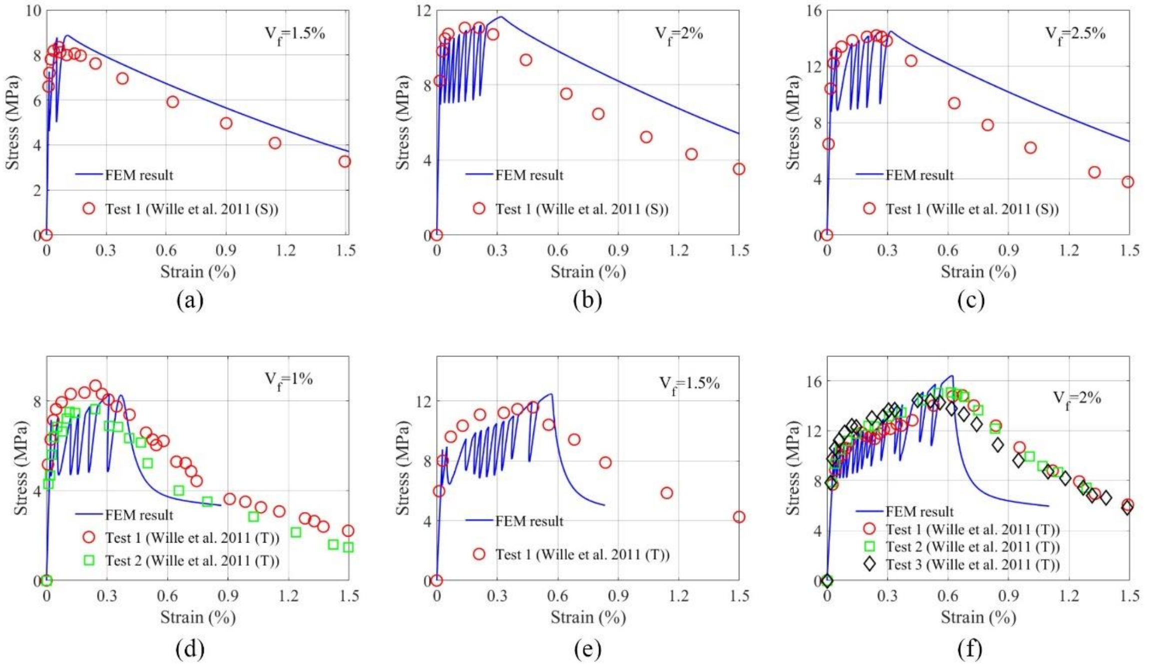

Fig. 3. Comparisons of the tensile stress—strain curves from FEM simulations and from experiments by Wille et al. (2011a), for UHPFRC reinforced with (a) 1.5%, (b) 2% and (c) 2.5% of straight steel fibers, and (d) 1%, (e) 1.5% and (f) 2% of twisted steel fibers.

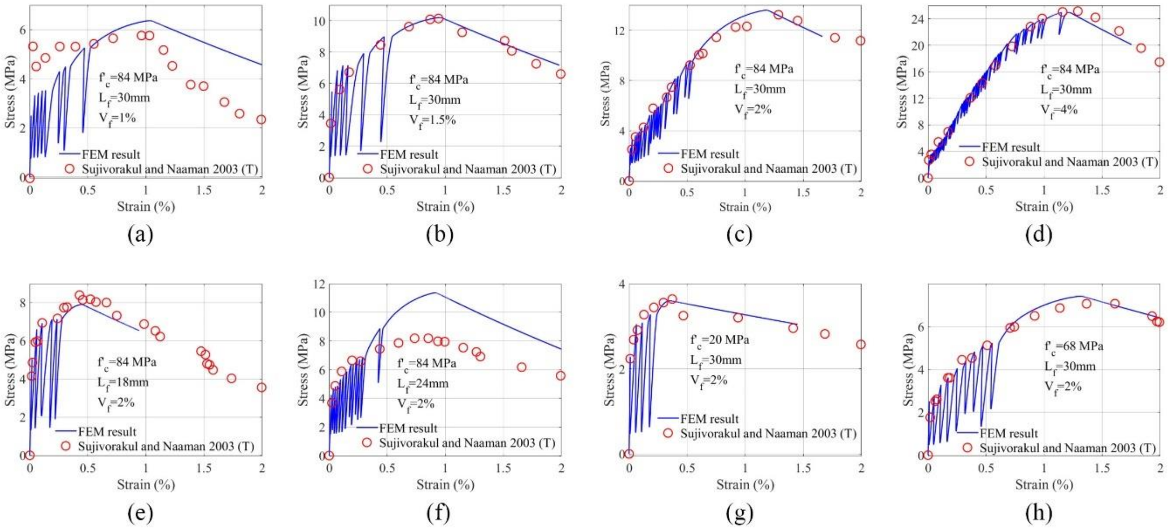

Fig. 4. Comparisons of the tensile stress—strain curves from FEM simulations and from experiments of Sujivorakul and Naaman (2003), for HPFRC having matrix compressive strength of $f'_c = 84\text{MPa}$ and (a) 1%, (b) 1.5%, (c) 2% and (d) 4% by volume of 30-mm long twisted steel fibers; for HPFRC having matrix compressive strength of $f'_c = 84\text{MPa}$ and 2% by volume of (e) 18-mm and (f) 24-mm long twisted steel fibers; for HPFRC having matrix compressive strength of (g) $f'_c = 20\text{MPa}$ and (h) $f'_c = 68\text{MPa}$ and 2% by volume of 30-mm long twisted steel fibers. The fiber diameter is $D_f = 0.3\text{mm}$ for cases (a)~(h).

Fig. 2 compares the stress—strain curves from FEM simulations and from tests by Wille et al. (2014) for both straight steel fiber-reinforced (Fig. 2 a~c) and twisted steel fiber-reinforced (Fig. 2 d~f) UHPFRC. It is shown that for all cases the simulated curves conform well with the tested ones in both strain-hardening and strain-softening stages. In Fig. 3, the FEM simulations are validated against the tensile tests of UHPFRC by Wille et al. (2011a), with lower fiber volume fraction ($\leq$ 2.5 %) and lower matrix compressive strength ($f'_c = 190$ MPa) compared to the tests in (Wille et al. 2014). For different cases, the starting point and the slope of the strain hardening stage, as well as the ultimate stress and ultimate strain were well predicted. Fig. 4 shows the predictability of the FEM model for matrix compressive strengths lower than 120 MPa, against the tests by Sujivorakul and Naaman (2003). The predicted stress—strain curves were shown to be highly consistent with the tested stress-strain curves for most cases, in terms of the starting point and the curvature of the strain hardening stage, the ultimate stress and the ultimate strain, as well as the softening slope, while the bad fittings in Fig. 4 (a and f) were reasonably taken as scatters.

4. Strength, ultimate strain and stress—strain models of UHPFRC

The parametric analyais was conducted with respect to the fiber length L_f, fiber diameter D_f, fiber volume fraction V_f, interfacial friction stress τ_0, mean matrix cracking strength σ_{mc}, and interfacial stiffness k_i, as summarized in Table E.3.

4.1 Strength model of UHPFRC

We note that regarding the mathematical forms of the strength and ultimate strain models, we first tried polynomial regressions up to the order of ± 2. Although the derived formula gave a very good accuracy against the model-generated data, they normally involved multiple terms and a lot of parameters, which are not friendly to engineers (Same issues exist for more complex machine learning, with linear regression as the simplest version). More importantly, they overfitted the experimental data, giving a bad robustness.

Physically, the post-cracking strength of UHPFRC should be zero (no strain hardening) when any of the parameters L_f, $1/D_f$, V_f or τ_0 reduces to zero, and thus a physical-consistent mathermatical form of the ultimate strength σ_{pc} of UHPFRC was assumed as follows:

$$\sigma_{pc}^{reg} = L_f^{e_1} D_f^{e_2} V_f^{e_3} \tau_0^{e_4} (a_1 + a_2 \sigma_{mc}^{e_5})(a_3 + a_4 k_i^{e_6}). \quad (12)$$

By using ridge regression (see Appendix D), the expression for σ_{pc}^{reg} was derived as follows:

$$\sigma_{pc}^{reg} = 1.33 \left(\frac{V_f L_f}{D_f} \right)^{0.68} \tau_0^{0.6} \sigma_{mc}^{0.29}. \quad (13)$$

It turns out that the composites strength σ_{pc} is independent of the interfacial stiffness k_i. Note that since there is no bias term in Eq. 12, the parameters in Eq. 13 were determined to minimize the mean absolute error (Eq. D6) against the model generated data without involving experimental data.

The quanlity of Eq. (13) was verified against the model-generated data in Fig. 5. It is shown that the regression model derived from the train data (Data 1~6 in Table E.3) sucessfully predicted the composites strengths which are consistent with the test data (Data 7~8 in Table E.3). Moreover, most of the data points are within the 85% prediction interval, and the mean absolute percentage error (MAPE) is 2.82%, indicating a good robustness of the model.

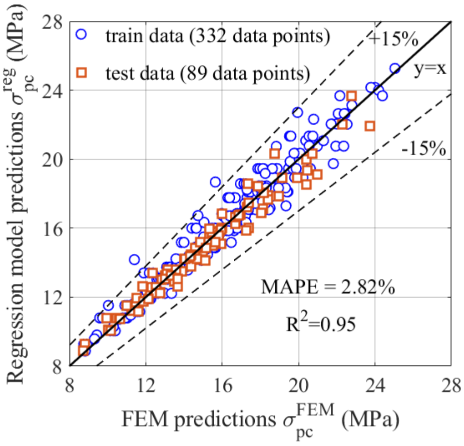

Fig. 5. Verification of the composite strength model against the FEM simulations.

To demonstrate the ability of Eq. (13) in predicting experimental data, the interfacial friction stress τ_0 needs to be determined which was usually not given in the experiments on UHPFRC. It was assumed that τ_0 is a function of the matrix compressive strength only:

$$\tau_0 = \begin{cases} 0.0474 f_c^{'}, \text{ for straight fiber} \\ 0.0632 f_c^{'}, \text{ for twisted fiber} \end{cases}, \quad (14)$$

which was derived by fitting Eq. (14) to the τ_0 values listed in Table E.2 and by fitting the predictions of Eq. (13) to the experimental data. $f_c^{'}$ is the compressive strength of the cement matrix. Different formulas were proposed for straight and twisted fibers in Eq. (14) because they have different surface shape and different interfacial strength even in the same matrix. The matrix cracking stress σ_{mc} used in the above fittings as listed in Table E.4 were all extracted from the tested stress—strain curves following the concept illustrated in Fig. B.1. To enable the application of the strength model in the real design and analysis of UHPFRC, we established an emperical relationship through data fitting (Wille et al. 2014) to relate the matrix cracking stress σ_{mc} to the fiber length L_f, diameter D_f, volume fraction V_f and matrix compressive strength $f_c^{'}$:

$$\sigma_{mc}^{reg} = 0.8 f_c^{'0.4} + 97.23 V_f . \quad (15)$$

Note that more rational formulas for σ_{mc} are also avaiable in the literature (Krstulovic-Opara and Malak 1997; Tjiptobroto and Hansen 1991, 1993a), which were derived based on the conservation of energy principle. Including them into the proposed model requires the additional definitions of matrix fracture energy and average elastic interfacial shear stress, the latter of which is usually unknown and is often determined emperically (Krstulovic-Opara and Malak 1997; Naaman et al. 1989). Hence we tentatively adopted Eq. (15) here. Fig. 6 (a) compares the predictions of Eq. (15) with the data extracted from experiments (see table E.4), showing a MAPE of 26.3% and a coefficient of determination is 0.463.

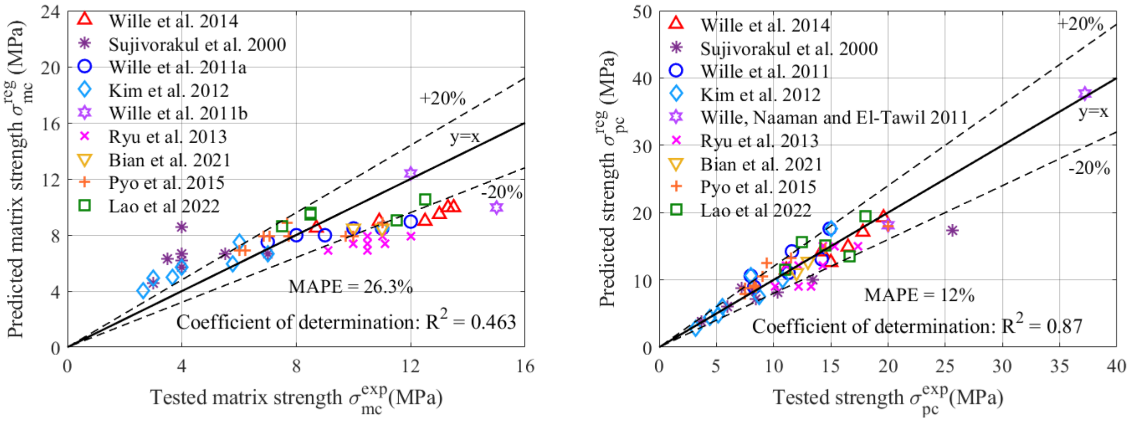

(a) (b)

Fig. 6. Validation of (a) the matrix strength model and (b) composites strength model of UHPFRC against experimental data.

Substituting equations (14) and (15) into Eq. (13), a utility model for the post-cracking strength of UHPFRC was derived:

$$\sigma_{pc}^{reg} = \begin{cases} 0.2135 RI^{0.68} f_c^{'0.6} \left(0.8 f_c^{'0.4} + 97.23 V_f\right)^{0.29}, \text{ for straight steel fiber} \\ 0.2537 RI^{0.68} f_c^{'0.6} \left(0.8 f_c^{'0.4} + 97.23 V_f\right)^{0.29}, \text{ for twisted steel fiber} \end{cases}, (16)$$

where RI is the reinforcing index which is defined as $V_f L_f / D_f$. The predictive ability of Eq. (16) is illustrated in Fig. 6 (b). The mean absolute percentage error of Eq. (16) is 12 % while the coefficent of determination is 0.87, indicating a good accuracy of Eq. (16) in predicting the ultimate strength of UHPFRC.

Here we explored the role of number and complexity of model-generated data on the quality of the derived strength model. The model-generated data as shown in Table E.3 were rearranged into groups I~VI with increasing level of number and complexity of data. Each group of data was individually used to derive a strength model. Corresponding model coefficients in Eq. 13 (denoted by $c_1 \sim c_4$ counted from the left), mean absolute persentage error (MAPE) and coefficient of determination (R^2) for the six models were summarized in Table 1. Note that since the interfacial stiffness k_i plays no role on the composite strength, group I data in Table 1 have no interactive variables (See Table E.3). It is seen that after group III, increasing the number and complexity of data leads to negligible improvements in the model accuracy. Besides, even group I of data, with only 51 data and no interactive variables, yields a reasonable accuracy of the strength model. Furthermore, with increasing number and complexity of data, the exponential coefficients of the model converge to constant values, demonstrating a good robustness of the model.

Table 1. Influence of data number and complexity on the quality of strength model

Group No.	I	II	III	IV	V	VI
Data sets	6	1, 2, 6	1, 2, 3, 6	1, 2, 3, 4, 6	1, 2, 3, 4, 5, 6	1, 2, 3, 4, 5, 6, 7, 8
Data amount	51	63	151	295	332	421
Interactive variables	None	None	$L_f - D_f - V_f - \tau_0$	$L_f - D_f - V_f - \tau_0$ $L_f - D_f - V_f - \sigma_{mc}$	$L_f - D_f - V_f - \tau_0$ $L_f - D_f - V_f - \sigma_{mc}$ $D_f - \tau_0 - \sigma_{mc}$	$L_f - D_f - V_f - \tau_0$ $L_f - D_f - V_f - \sigma_{mc}$ $D_f - \tau_0 - \sigma_{mc}$ $D_f - V_f - \sigma_{mc}$

						$V_f-\tau_0-\sigma_{mc}$
c_1	1.4411	1.4054	1.4940	1.4666	1.3935	1.3300
c_2	0.61	0.63	0.68	0.68	0.68	0.68
c_3	0.60	0.60	0.58	0.56	0.59	0.60
c_4	0.26	0.27	0.26	0.29	0.28	0.29
MAPE	0.124	0.122	0.120	0.120	0.119	0.119
R^2	0.852	0.860	0.877	0.879	0.874	0.872

4.2 Ultimate strain model of UHPFRC

The worse correlation between ultimate strain of UHPFRC with its constituent parameters suggested a more complicated form of the ultimate strain model:

$$\varepsilon_{pc}^{reg}=L_f^{\ e_1}D_f^{\ e_2}V_f^{\ e_3}\left(a_1+a_2\tau_0^{\ e_4}\right)(a_3+a_4\sigma_{mc}^{\ e_5})(a_5+a_6k_i^{\ e_6})\text{ . (17)}$$

By using ridge regression (see Appendix D), the ultimate strain model was derived as:

$$\varepsilon_{pc}^{reg}=\left(\frac{V_fL_f}{D_f}\right)^{0.38}k_i^{-0.3}\sigma_{mc}^{\ -0.22}\left(17.24-18.79\tau_0^{\ -0.5}\right)\text{. (18)}$$

The quality of Eq. (18) is illustrated in Fig. 7 (a), where predictions of Eq. (18) were compared with the ultimate strain data from FEM simulations. Although the mean absolute error was as small as 9.8%, the Eq. (18) overstimated some of the test data (mostly from Data 7). Substituting Eqs. (14) and (15) into Eq. (18), we have:

$$\varepsilon_{pc}^{reg}=\begin{cases}\left(\dfrac{V_fL_f}{D_f}\right)^{0.38}k_i^{-0.3}\left(0.8f_c^{'0.4}+97.23V_f\right)^{-0.22}\left(17.24-86.31f_c^{'-0.5}\right)\text{, for straight steel fiber}\\ \left(\dfrac{V_fL_f}{D_f}\right)^{0.38}k_i^{-0.3}\left(0.8f_c^{'0.4}+97.23V_f\right)^{-0.22}\left(17.24-74.74f_c^{'-0.5}\right)\text{, for twisted steel fiber}\end{cases}\text{, (19)}$$

Since the interfacial stiffness k_i is a material parameter unavaiable in the experiments, k_i was assumed to be a function of the matrix compressive strength $f_c^{'}$ only. By fitting Eq. (19) to the experimental data, the funciton $k_i(f_c^{'})$ was obtained as follows:

$$k_i = \begin{cases} 880\sqrt{f_c^{'}}, & \text{if } f_c^{'} \geq 120\text{MPa} \\ 220\sqrt{f_c^{'}}, & \text{if } f_c^{'} < 120\text{MPa} \end{cases}, \quad (20)$$

Substituting Eq. (20) into Eq. (19) leads to:

$$\varepsilon_{pc}^{reg} = \begin{cases} \alpha RI^{0.38} f_c^{'-0.15}\left(0.8 f_c^{'0.4} + 97.23V_f\right)^{-0.22}\left(17.24 - 86.31 f_c^{'-0.5}\right), \text{ for straight steel fiber} \\ \alpha RI^{0.38} f_c^{'-0.15}\left(0.8 f_c^{'0.4} + 97.23V_f\right)^{-0.22}\left(17.24 - 74.74 f_c^{'-0.5}\right), \text{ for twisted steel fiber} \end{cases}, \quad (21)$$

where *RI* is the fiber reinforcing index, and α was defined as follows:

$$\alpha = \begin{cases} 0.1308, & \text{if } f_c^{'} > 120\text{MPa} \\ 0.1983, & \text{if } f_c^{'} \leq 120\text{MPa} \end{cases}. \quad (22)$$

It is noted that although Eq. (20) leads to much higher interfacial stiffnesses (e.g., 13346 MPa/mm for $f_c^{'}$ of 230 Mpa) than those listed in Table E.2 (e.g., 4000 Mpa/mm for $f_c^{'}$ of 230 Mpa), it provides the best overall performance in fitting all the exprimental data, as illustrated in Fig. 7 (b). The mean absolute error (MAE) is 0.16 while the mean absolute persentage error is 40.7 (MAPE). Note that when calculating MAE and MAPE, the cases with ultimate strain lower than 0.1, which is deemed as strain softening, were not accounted for. Moreover, when only the cases for ultimage strain higher than 0.2 or 0.3 were considered, the corresponding MAPE reduced to 33.1% and 25.3%, respectively. This means that the present ultimate strain model is more accurate in predicting the tensile response of UHPFRC with good strain hardening performance. The reason for this is that the FEM model assumed that the matrix strength is close to the mean value σ_{mc} at all sections of the specimen, and thus the specimen is able to deform until cracks interact even when fiber bridging strength approaches matrix strength. However, in reality the matrix strength varies to a certain degree, so the specimen fails quickly when the bridging strength approaches the minimum matrix strength, leading to a more brittle behavior than the case of more uniform matrix strength distribution.

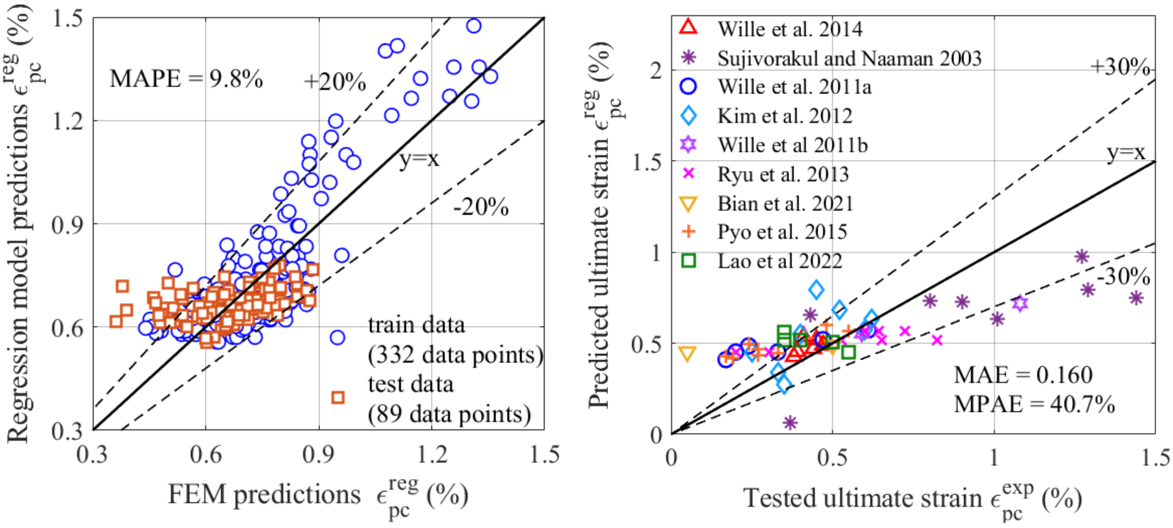

Fig. 7. Verification of the composite ultimate strain model against (a) the FEM simulations and (b) experimenta data.

Table 2. Influence of data number and complexity on the quality of ultimate strain model

Group No.	I	II	III	IV	V	VI
λ	0.0001	0.0001	0.0002	0.0002	0.0004	0.001
d_5	15.06	15.81	16.14	17.02	17.23	17.24
d_6	-17.21	-18.32	-16.12	-17.71	-18.37	18.79
MAPE	0.346	0.360	0.392	0.413	0.414	0.407
R^2	0.350	0.372	0.482	0.472	0.465	0.458

We further investigated the sensivity of the model accuracy to the amount and complexity of data following the procedure presented in Section 4.1. The derived ultimate strain model does not convergence with respect to the coefficients in Eq. 18 (denoted by $d_1 \sim d_6$ counted from the left). However, when the exponential coefficients $d_1 \sim d_3$ and d_6 are fixed as those shown in Eq. 18, the parameters d_4 and d_5 can be determined to consistently give a ultimate strain model which predict well model-generated data and experimental data simultaneously using different amount and complexity of data. This requires to choose an appropriate regularization parameter λ by fitting to experimental data. The parameters $d_5 \sim d_6$, λ, MAPE and coefficient of determination (R^2) are summarized in Table 2. Surprisingly, the model which gives the minimum MAPE is generated from data group I, while data group III leads to the highest coefficient of determination. Therefore, it can be inferred that, a general robust procedure to derive a resonable ultimate strain model of UHPFRC based on the given mathematical form is to loop over the exponential parameters and regularization parameter λ, and the suitable set of parameters can be found that predict best the experimental data. It should be noted that the suitable mathematical forms of the strength or ultimate strain model are not unique. The numerical data filters out the uncertainties during experiments, while the experimental data pull the numerical model back to reality by relax simplistic assumptions to some degree.

4.3 Stress—strain model of UHPFRC

The stress—strain model was estabilished based on the strength model developed in Section 4.1 and ultimate strain model in Section 4.2. Furthermore, to define the softening branch of the stress—strain curve, the strain ε_{pc14} corresponding to the residual strength σ_{pc14} of 1/4 the ultimate strength σ_{pc}^{reg} of UHPFRC was derived through ridge regression. Group data I was used in the derivation which was demonstrated in Section 4.1 and 4.2 to be sufficient for deriving both reasonable strength and ultimate strain models. By assuming the same mathematical form as Eq. 18, ε_{pc14} was derived as follows:

$$\varepsilon_{pc14}^{reg} = 20.92\left(\frac{L_f}{D_f}\right)^{-0.28} k_i^{-0.14}. \quad (23)$$

Eq. 23 was verified against group I of data in Fig. 8. Despite the simple form of Eq. 23, its robustness is reasonable against FEM model, featuring a mean absolute persentage error of 5.88% and coefficient of determination of 0.755. A unified form of $k_i = 220\sqrt{f_c^{'}}$ instead of Eq. 20 was substituted into Eq. 23 leading to:

$$\varepsilon_{pc14}^{reg} = 9.83\left(\frac{L_f}{D_f}\right)^{-0.28} f_c^{'-0.07} \text{.(24)}$$

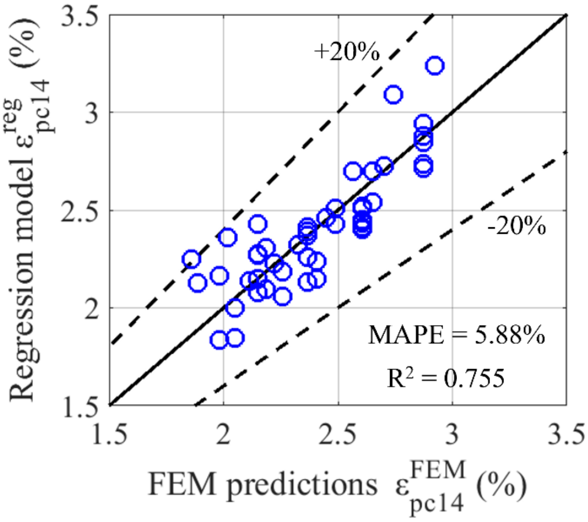

Fig. 8. Verification of the strain model ε_{pc14}^{reg} corresponding to σ_{pc}^{reg}/4 residual strength against the group I of FEM data.

The elastic modulus of UHPFRC was determined merely by the rule of mixture, which was written as:

$$E_c = (1 - V_f)E_m + V_f E_f \text{ . (25)}$$

Following Wille et al. (2014), the matrix Young's Modulus was calculated by:

$$E_m = 9150\left(f_c^{'}\right)^{\frac{1}{3}} \text{. (26)}$$

A multi-linear stress—strain model for UHFPRC was proposed as follows:

$$\sigma = \begin{cases} E_c \varepsilon, & \text{if } \varepsilon < \varepsilon_{fc} \\ \sigma_{fc} + E_{sh}(\varepsilon - \varepsilon_{fc}), & \text{if } \varepsilon_{fc} \le \varepsilon < \varepsilon_{mc} \\ \sigma_{mc}^{reg} + E_{wh}(\varepsilon - \varepsilon_{mc}), & \text{if } \varepsilon_{mc} \le \varepsilon < \varepsilon_{pc}^{reg} \\ \sigma_{pc}^{reg} + E_{sf}(\varepsilon - \varepsilon_{pc}^{reg}), & \text{if } \varepsilon_{pc}^{reg} \le \varepsilon \end{cases} \text{, (27)}$$

in which σ_{fc} and ε_{fc} are the first cracking stress and first cracking strain, respectively, and were defined as follows:

$$\sigma_{fc} = 0.8\left(f_c^{'}\right)^{0.4} \text{, (28)}$$

$$\varepsilon_{fc} = \frac{\sigma_{fc}}{E_c}, \quad (29)$$

E_{sh} is the hardening modulus at the swift strain hardening stage:

$$E_{sh} = \frac{\sigma_{mc}^{reg} - \sigma_{fc}}{\varepsilon_{mc} - \varepsilon_{fc}}, \quad (30)$$

E_{wh} is the hardening modulus at the wildely held strain hardening stage:

$$E_{wh} = \frac{\sigma_{pc}^{reg} - \sigma_{mc}^{reg}}{\varepsilon_{pc}^{reg} - \varepsilon_{mc}}, \quad (31)$$

and E_{sf} is the softening modulus at the strain softening stage:

$$E_{sf} = \frac{-3\sigma_{pc}^{reg}}{4(\varepsilon_{pc14}^{reg} - \varepsilon_{pc}^{reg})}. \quad (32)$$

σ_{mc}^{reg}, σ_{pc}^{reg}, ε_{pc}^{reg} and ε_{pc14}^{reg} are defined in Eqs. (15), (13), (21) and (24) respectively. ε_{mc} is defined as the mean matrix cracking strain or the strain at which the widely held strain hardening stage starts, and is set to be 0.05 % according to the tested tensile stress—strain curves of UHPFRC presented in the literature.

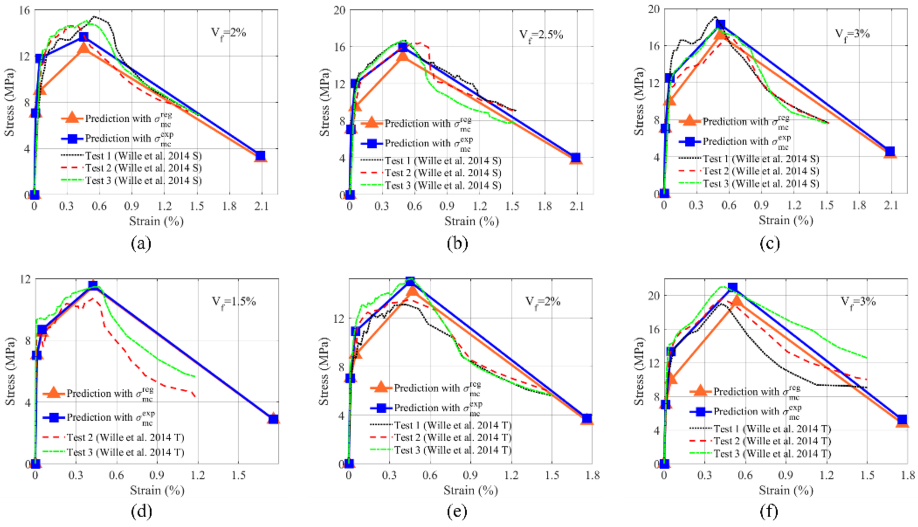

(a) (b) (c)

(d) (e) (f)

Fig. 9 Stress—strain curves predicted by the present model versus those tested by Wille et al. (2014)

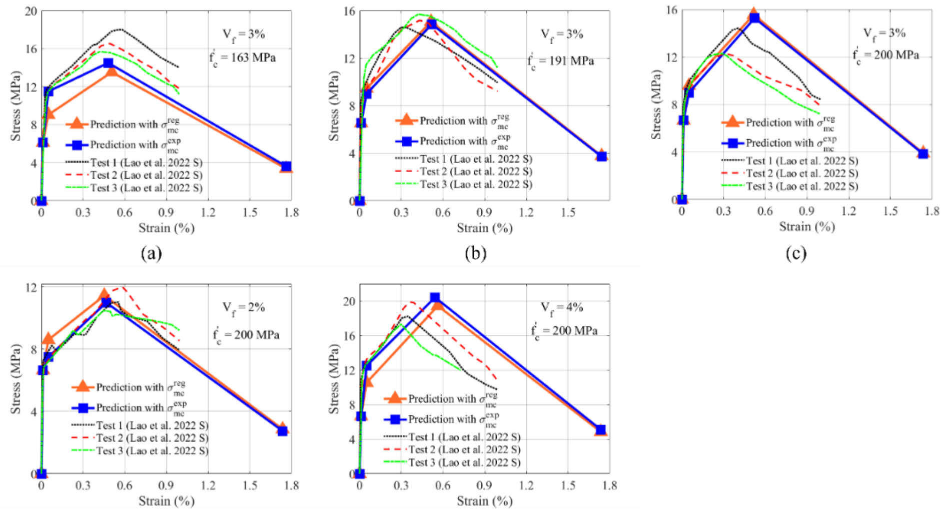

(a) (b) (c)

(d) (e)

Fig. 10 Stress—strain curves predicted by the present model versus those tested by Lao et al. (2022).

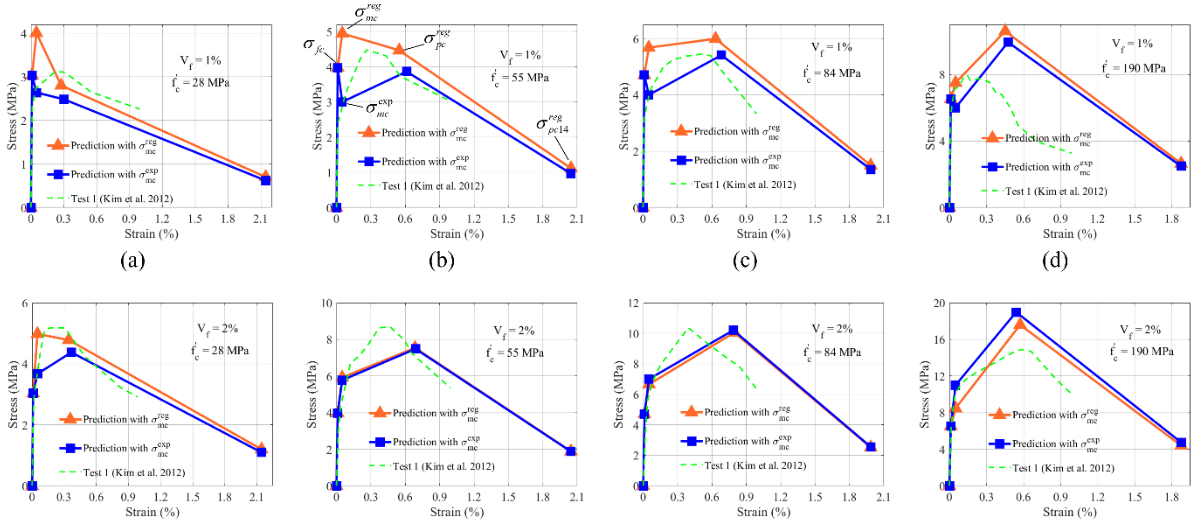

(a) (b) (c) (d)

(e) (f) (g) (h)

Fig. 11 Stress—strain curves predicted by the present model versus those tested by Kim et al. (2012).

The validity of the multi-linear stress—strain model (Eq. 27) was examined by the tested stress—strain curves from (Kim et al. 2012; Lao et al. 2022; Wille et al. 2014), as illustrated in Fig. 9, 10 and 11, where the stress—strain curves predicted by replacing σ_{mc}^{reg} with $\sigma_{mc}^{\exp}$ (values extracted from experiments as listed in Table E.4) are also illustrated as a reference. It is shown that for UHPFRC (with matrix compressive strength $f_c^{'} \geq 120\text{MPa}$), i.e., Fig. 9 (a~f),

Fig. 10 (a~f) and Fig. 11 (d and h), the stress—strain curves predicted by Eq. (27) conformed well with the stress—strain curves tested in the experiments for most cases. Moreover, by replacing the σ_{mc}^{reg} in Eq. (27) with the mean matrix cracking stress $\sigma_{mc}^{\exp}$ extracted from the tested curves, the predictions fitted much better with the tests, in terms of the slopes of the swift strain hardening stage and the widely held strain hardening stage, as well as the ultimate strength and ultimate strain of the UHPFRC. This suggested that the further improvement in the present stress—strain model should be targeted at developing a more accurate model to predict the mean matrix cracking stress σ_{mc}, and understanding the underlying physical mechanisms, through both experimental and numerical tools. Regarding the softening branch, almost in all cases the predicted softening slopes agree well with experimenta results, although Eq. (23) was derived using the group I of FEM data only without enhanced by any experimental data. On the other hand, regarding HPFRC with matrix compressive strength $f_c^{'} < 120\text{MPa}$, for which the predictions were compared with tests in Fig. 11 (a~c and e~f), the quality of the predicted stress—strain curves is relatively poor compared to that for matrix compressive strengths higher than 120 MPa, although the ultimate conditions may be well reproduced. Particularly, in Fig. 11 (a, b and e), the predicted mean matrix cracking stresses σ_{mc}^{reg} exceed the predicted ultimate strengths σ_{pc}^{reg} of UHPFRC, indicating strain softening (indicated by decrease in stress after matrix cracking), which is in conflict with the experiments.

By plotting $\sigma_{pc}^{reg} - \sigma_{mc}^{reg}$ (Difference between σ_{pc}^{reg} and σ_{mc}^{reg}) surfaces in the $(RI, f_c^{'})$ space for different values of fiber volume fraction V_f as shown in Fig. 12, it can seen that σ_{mc}^{reg} turns to be larger than σ_{pc}^{reg} for smaller values of RI, $f_c^{'}$ and V_f. This is because the proposed Eq. (15) for σ_{mc}^{reg} overestimate the real $\sigma_{mc}^{\exp}$ for lower $f_c^{'}$ values (see Fig. 6). Even using $\sigma_{mc}^{\exp}$, the predicted ultimate strength σ_{pc}^{reg} is lower than $\sigma_{mc}^{\exp}$ in Fig. 11(a), which has the lowest RI, $f_c^{'}$

and V_f in all examined tests. This issue can be solved by replacing Eq. (14) with a more accurate yet more complex model of τ_0, which is beyond the scope of this work. As acompensation, it is suggested that when σ_{pc}^{reg} is predicted to smaller than σ_{mc}^{reg}, the σ_{mc}^{reg} calculated by Eq. (15) should be adjusted to be equal to σ_{pc}^{reg}, considering that Eq. (13) for σ_{pc}^{reg} is more rational and physics-based. Similarly, σ_{fc} given by Eq. (28) should be adjusted to when larger than the value of σ_{mc}^{reg}.

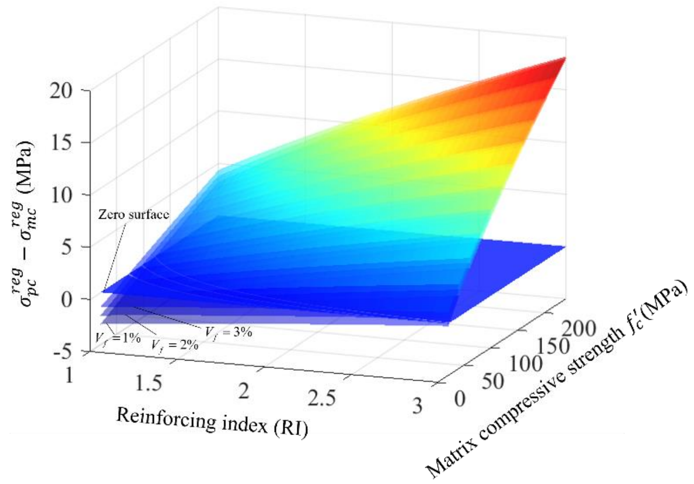

Fig. 12 $\sigma_{pc}^{reg} - \sigma_{mc}^{reg}$ surfaces in the $(RI, f_c^{'})$ space for different fiber volume fractions (V_f)

Overall, accurately capturing the mean matrix cracking strength is very important in proper predictions of the strain hardening behavior of HPFRC with matrix compressive strength lower than 120 MPa, expecially for strain hardening FRC with both low fiber content and low matrix compressive strength, i.e., Fig. 11 (a) and (b). It is worth noting that the present model was developed for cementitious composites reinforced by steel fibers only. For extending the present framework to tensile stress—strain model of cementitious composites reinforced by other fiber types, e.g., PVA fiber, PE fiber, carbon fiber, the FEM model adopted here can still be used. However, the unified parameters should be carefully redefined according to corresponding direct tensile test results, since different fiber types exhibit distinct fiber

Young's Modulus, tensile strength σ_f^y, orientation distribution FOD, strength reduction coefficient f'; interface hardening parameter and snubbing coefficient. Besides, the range of the specific variables of interests differ significantly for different fiber types. As for hybrid fiber composites, the FEM model remains to be modified to include more fiber types, which is straightforward.

It is interesting to notice that in the present model, the higher mean matrix cracking stress σ_{mc} gave a noticably higher ultimate strength (see tested results in Fig. 2 b~f and predicted results in Fig. 9, 10 and 11, and also see Eq. (13) and (18)) of UHPFRC as well as a less noticeable lower ultimate strain of UHPFRC (see Fig. 9, 10 and 11, and Eqs. (13) and (18)). However, it is commonly expected that the ultimate strength of UHPFRC is determined by the fiber orientation distribution, fiber volume fraction, fiber length, fiber diameter and interfaical friction stress only. This is only valid in single cracking tests. Although Liu et al. (2022) identified that the residual compressive tractions at crack surfaces for strain hardening cementitious composites experiencing multiple crackings may reduce the composites strength, Liu et al. also claimed that the UHPFRC is free from this effect. This is because the high interfacial unloading stiffness in UHPFRC helps release fiber stress upon crack closing and the relatively sparse distribution of cracks alleviates the development of compressive tractions on crack surfaces. The underlying mechanisms were elaborated in the next section.

5. Influence of mean matrix cracking stress and microstress analysis

A parametric analysis was first conducted with respect to the mean matrix cracking stress σ_{mc}, the parameters adopted in the analysis were the unified parameters listed in Table E.2 and the specific parameters listed in Table E.5. The simulated stress—strain curves for various mean matrix cracking stress σ_{mc} were compared in Fig. 13. It was found that the predicted composite ultimate strength (13 MPa, 13.8 MPa, 14.8 MPa and 15.3 MPa, respectively) increases with the mean matrix cracking stress (8 MPa, 10 MPa, 12 MPa and 14 MPa, respectively), while the ultimate strain was not obviously affected in these cases. Moreover, for lower mean matrix cracking stress, there were more cracks at different stages, characterized by the denser stress fluctuations in the stress—strain curves.

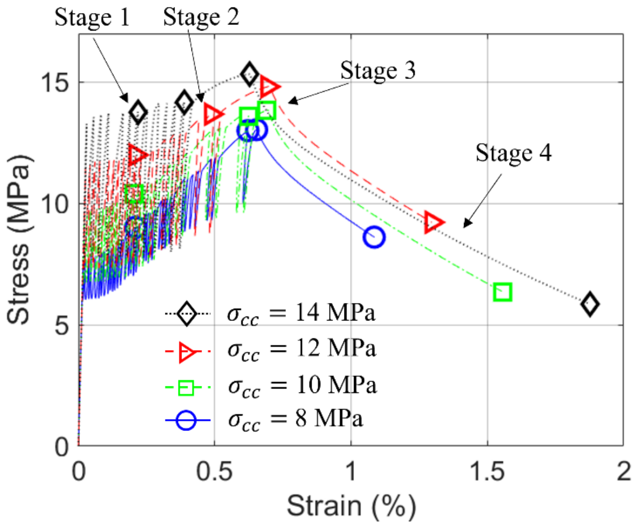

Fig. 13 Comparison of the stress—strain curves for different matrix cracking stresses σ_{mc} .

To identify the reasons behind the above observations, the distributions of the interfaical stresses for fibers oriented at 5 different angles (22.6°, 32.2°, 46.2°, 52°and 62.5°, i.e., the angles adopted in the FEM simulations), which have their centers on the final localized crack (represented by the grey dashed line), are presented and compared in Fig. 14, for the mean matrix cracking stresses of 8 MPa, 10 MPa, 12 MPa and 14 MPa, respectively. The crack widths of the activated cracks at different stages are also presented in Fig. 14, where the stage 1, stage 2 and stage 3 correspond to the data points as illustrated in Fig. 13. Particularly, the stage 1 represents the stage at the applied strain of approximately 0.2 %, the stage 2 represents the state right before the final crack initiates, the stage 3 represents the peak stress point, and the stage 4 represents the state when strain softening happens. All the stages are at the upper profile of the stress—strain curve.

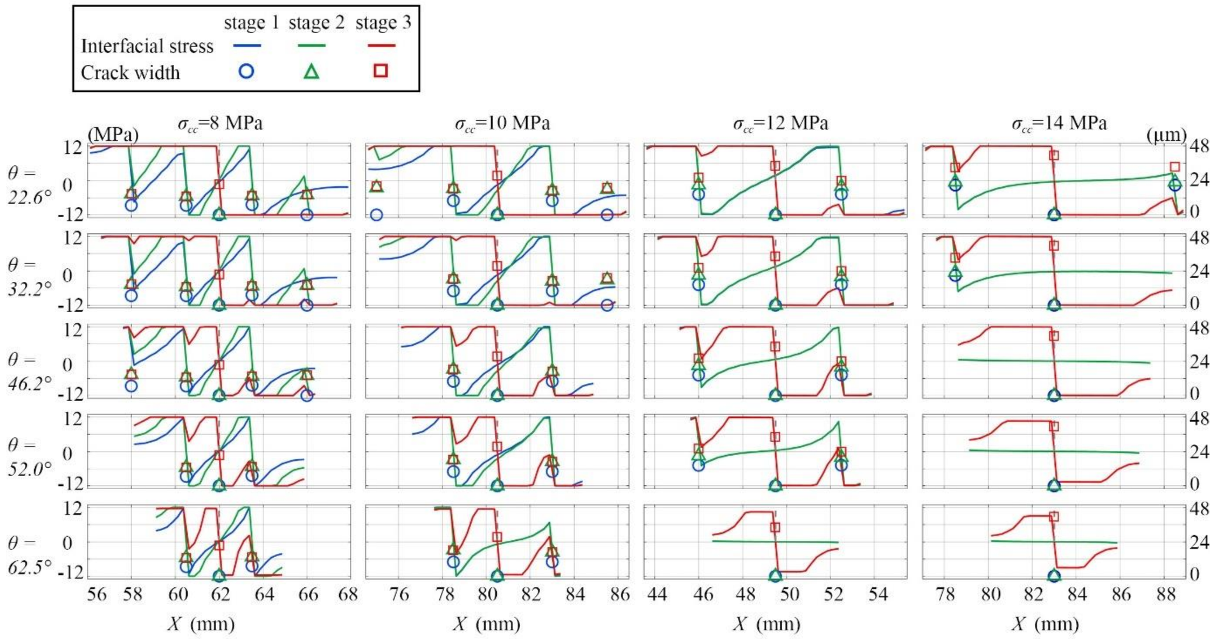

Fig. 14. Profiles of the interfacial stresses and crack widths corresponding to different mean matrix cracking stresses.

Clearly, the lower is the mean matrix cracking stress, the more cracks are crossed by the fibers oriented at different angles. This caused significant differences in the profiles of the interfacial stress distributions at stage 1 and stage 2, for different mean matrix cracking stresses. Particularly, there were more waves in the profiles of interfacial stresses for fibers which cross more cracks. Besides, the interfacial stress turned the sign going from one crack to the closely neighbored adjacent crack, and the turning point was approximately in the middle of the two cracks in most cases. Interestingly, at the peak stress state (Stage 3), when the major crack has the largest crack opening, the waves in the profiles of the interfacial stress were mostly straightened, and the profiles of the interfacial stress became quite similar for different mean matrix cracking strengths. Therefore, it was concluded that it was not the differences in the interfacial stress profiles which majorly contributed to the different composite ultimate strengths. Noticing that the peak interfaical stresses at stage 3 were found to be below 12 MPa for fibers inclined at 62.5° in the matrix with cracking stresses of 12 and 14 MPa, which is unusual. This is because those fibers were at the softening state due to fiber rupture.

Recalling Eq. (7), and considering that the cement matrix is brittle which means zero matrix tractions on active cracks at stage 1~4, the applied stress should be equal to the composite bulk stress σ_c and be determined by the fiber bridging stress $\left(\sigma_I^J\right)_{i_\Gamma}$ only, whose evolution was expressed by Eq. (10). Herein, the fiber bridging stress $\left(\sigma_I^J\right)_{i_\Gamma}$ was divided into two parts: the normal fiber stress σ_I^J contributed by normal interfacial friction, and the snubbing stress $\left(\sigma_I^J\right)_{i_\Gamma}^{snubbing}$ which was contributed by the intense friction at the fiber exist point (i.e., snubbing effect) with respect to the crack i_Γ, and was defined as:

$$\left(\sigma_I^J\right)_{i_\Gamma}^{snubbing} = \left(\sigma_I^J\right)^{active}\left(e^{f\theta^J} - 1\right). \quad (33)$$

Therefore, $\left(\sigma_I^J\right)_{i_\Gamma}^{snubbing}$ is proportional to the part of fiber stress $\left(\sigma_I^J\right)^{active}$ which is developed after the crack i_Γ is activated, and thus the fiber bridigng stress $\left(\sigma_I^J\right)_{i_\Gamma}$ should also increase with $\left(\sigma_I^J\right)^{active}$ provided that the σ_I^J is fixed.

Fig. 15 compared the profiles of fiber stresses σ_I^J at stages 1~4 for the mean matrix cracking stresses of 8, 10, 12 and 14 MPa, respectively. Clearly, the fiber stresses at the localized crack (dashed line) are quite similar with respect to different mean matrix cracking stresses, regardless of the fiber inclination angles (the cases where fiber ruptured at stage 3 were not considered in this analysis, i.e., $\left(\theta, \sigma_{mc}\right) = \left(52^\circ, 14\text{MPa}\right)$, $\left(62.5^\circ, 12\text{MPa}\right)$ and $\left(62.5^\circ, 14\text{MPa}\right)$). However, it was found that the lower mean matrix cracking stress σ_{mc} led to the higher fiber stress $\left(\sigma_I^J\right)^{inactive}$ at the localized crack at stage 2 (the stage right before the final localized crack was initiated). Recalling Eq. (11), Eq. (33) and Eq. (8), this explained why the fiber stress developed after crack activation $\left(\sigma_I^J\right)^{active}$ (see Fig. 15), the snubbing stress

$\left(\sigma_I^J\right)_{i_\Gamma}^{snubbing}$ (see Fig. 15), and in turn the composites ultimate strength decrease with the decrease of mean matrix cracking stress.

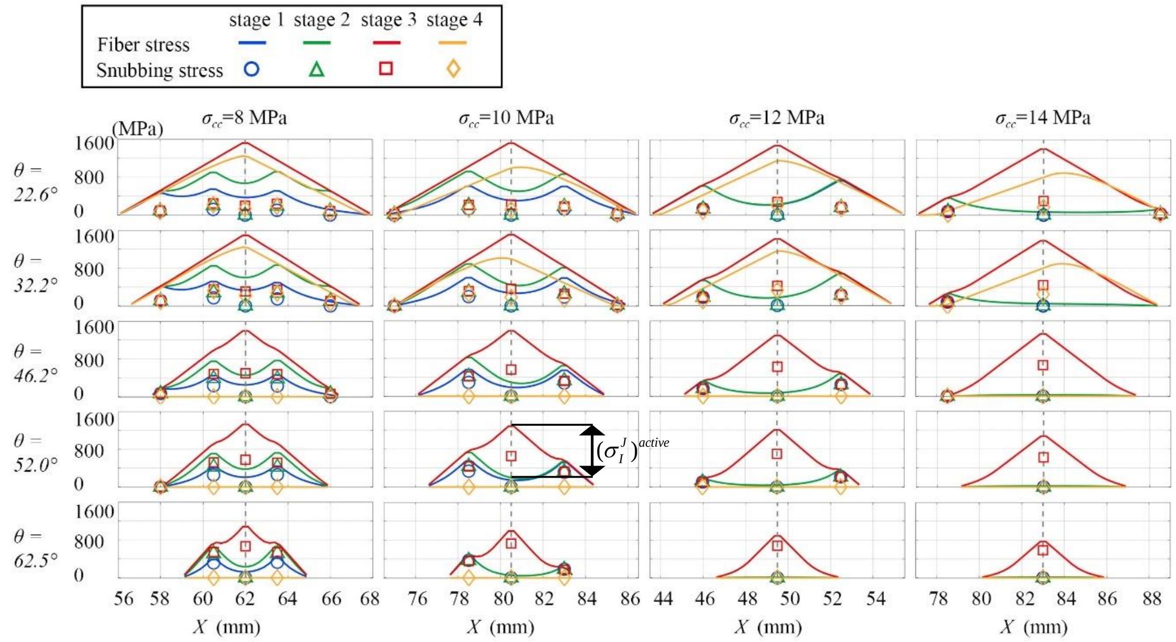

Fig. 15. Profiles of the fiber stresses and snubbing stresses corresponding to different mean matrix cracking stresses.

Another interesting finding is that the ultimate strains (see Fig. 13) for different mean matrix cracking stresses were close to each other, even though significantly different number of cracks formed at the ultimate state, i.e., 38, 28, 19, 13 cracks for the mean matrix cracking stresses of 8 MPa, 10 MPa, 12 MPa and 14 MPa, respectively (see Fig. 17a). Accordingly, the mean crack width at the ultimate state (stage 3) were 12.8 μm, 19 μm, 27.2 μm and 35.4 μm, for mean matrix cracking stresses of 8 MPa, 10 MPa, 12 MPa and 14 MPa, respectively (see Fig. 15a), although the differences in the ultimate strengths were found to be much less significant. Particularly, Fig. 15 (b) illustrated that at the same applied stress of 12.5 MPa, the average crack width decreases with the increase of crack density. Moreover, when the applied stress increased from 12.5 MPa to the ultimate stress, the higher the mean matrix cracking stress (or lower crack densities) is, the more the mean crack widths increases, with the the mean crack width for $\sigma_{mc} = 12\text{MPa}$ almost doubling. By refering to the fiber bridigng stress—crack width curve (σ—δ) as shown in Fig. 18, the higher the mean matrix cracking stress is (lower crack densities), the more similar is the applied stress—mean crack width relationship to the σ—δ curve, which further highlighted significance of multi-crack interactions in the study of UHFPRC.

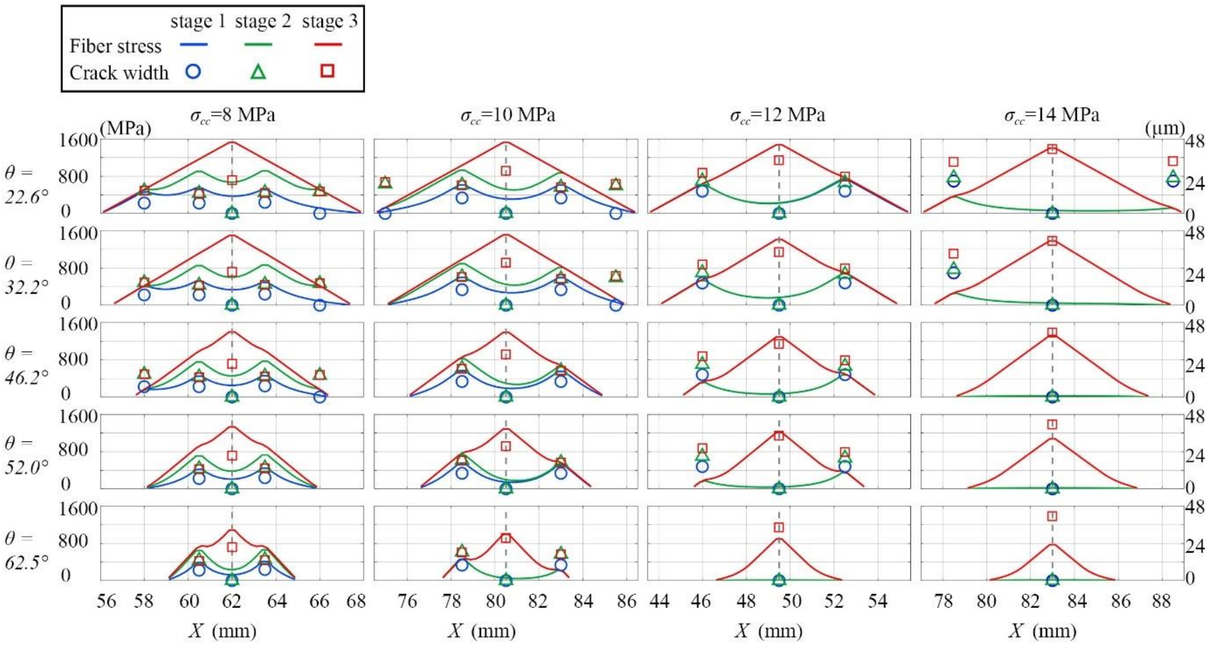

Fig. 16. Profiles of the fiber stresses and the crack widths corresponding to different mean matrix cracking stresses.

To understand the underlying mechanisms behind the above-mentioned observations, the evolutions of fiber stresses together with the crack widths were presented and compared in Fig. 16 for different mean matrix cracking stresses. Let's focus on the case for mean matrix cracking stress of 8 MPa. From stage 2 to stage 3, when a new crack initiated and opened between two old cracks, the fiber stresses (See Fig. 16) and the snubbing stresses (See Fig. 15) at the old cracks were upgraded to noticeable higher levels, without any visible increase in the crack widths (See Fig. 16) of the old cracks, although the width of the new crack is higher than that of old cracks. The origin for this is that the initiation and opening of the new crack changed a lot the interfacial stress profiles in the vicinity of the adjacent old cracks (See. Fig. 14). Such process happened many times in the low-cracking-stress matrix ($\sigma_{mc} = 8\text{MPa}$) which had more cracks, but was much less observed in high-cracking stress matrix ($\sigma_{mc} = 14\text{MPa}$) as illustrated in Fig. 16. Overall, the lower mean matrix cracking stress leads to the slightly lower composite strength, significantly higher number of cracks and much smaller average crack width at the ultimate state. This further suggested that to establish a reliable model for the tensile cracking characteristics of UHPFRC, an accurate model for the prediction of the mean matrix cracking stress σ_{mc} is in demand.

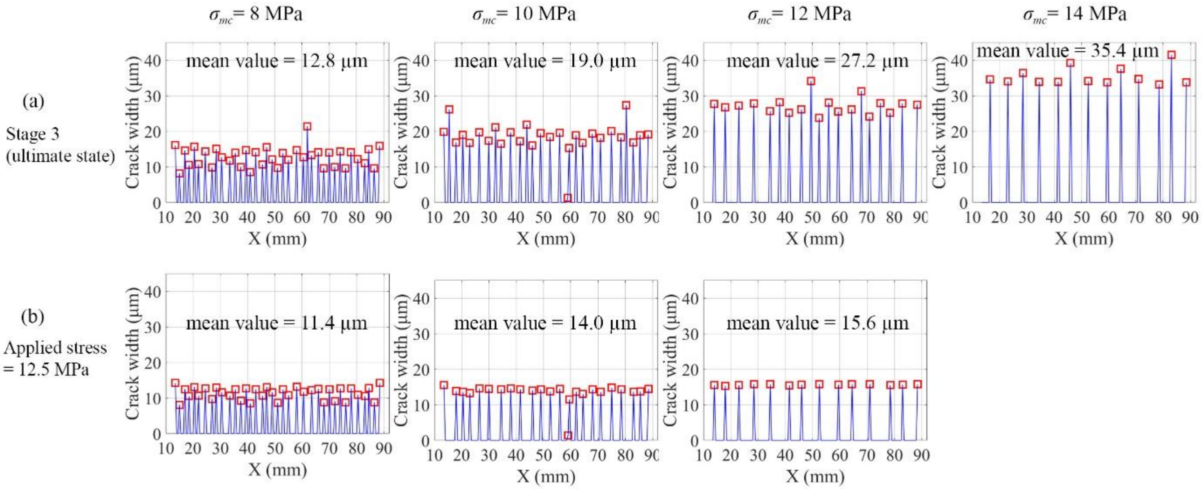

Fig. 17. Comparison of the crack width disbritutions at ultimate state (a) and at the applied stress of 12.5 MPa (b) for different mean matrix cracking strengths. Note that all data points were chosen on the upper profile of the stress—strain curves shown in Fig. 11.

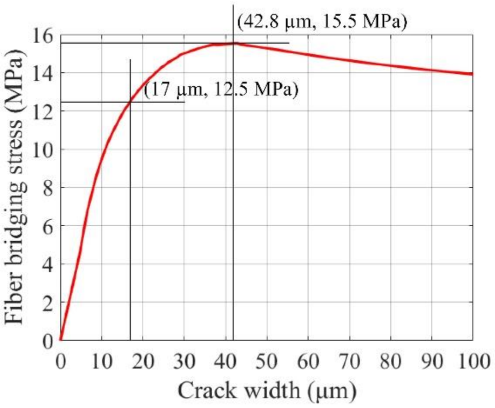

Fig. 18. Bridging stress versus crack width relationship obtained by the single cracking FEM simulation.

6. Applicability

Two potential applications of the present stress-strain model can be proposed. The first one is on using the proposed model for design purpose, i.e., designing UHPFRC with appropriate first cracking stress, ultimate strength and ultimate strain according to practical needs. Considering that the proposed model has been validated with test data for both traditional low strength (a minimum of 28 MPa (Kim et al. 2012)) and high strength (a maximum of 230 MPa (Wille et al. 2014)) concrete as well as geopolymer concrete (Lao et al. 2022), there should be no restrict on the type of cement composition.

Regarding the fiber type, straight and twisted steel fibers are directly applicable to the present model. Other types of steel fibers such as crimped or hooked fiber may also be applicable, but appropriate formulas should be proposed to relate the interfacial shear stress to the matrix compressive strength. Special care should be taken when using the proposed model for hooked steel fiber reinforced concrete, since it has significantly higher shear stress transfer around the hook due to mechanical locking, which contradicts with the uniform interfacial shear strength assumption in the FEM.

Given the matrix compressive strength and interfacial shear stress as a function of the matrix compressive strength, the range of the fiber aspect ratio and fiber content within which the present model is applicable can be determined by Eq. (18) and Eq. (15) such that $\sigma_{\mathrm{pc}}^{reg} > \sigma_{mc}^{reg}$, which is a necessary condition for strain hardening to occur. A simpler formula can be derived by equating Eq. (13) to σ_{mc}, such that the single cracking strength of UHPFRC is obtained:

$$\sigma_{sc} = \exp\left(\frac{1}{0.71} \log(1.31 RI^{0.68} \tau_0^{0.6}) \right) = 4.09^{\log(1.31 RI^{0.68} \tau_0^{0.6})}, \quad (34)$$

and the strain hardening criterion in the present framework becomes $\sigma_{sc} > \sigma_{mc}^{reg}$.

The applicable range of fiber tensile strength also matters. In all the FEM simulations we have assumed a constant fiber tensile strength of 3000 MPa, because the rupture of steel fiber was hardly encountered according to reports from extensive experimental works. Usually failed fibers are those with high aspect ratio, high interfacial strength and high inclination angles, thus constituting a very small portion of the bridging fibers. Typical cases are twisted fibers embedded in high strength cement matrix such as in Fig. 2 (d, e and f) and Fig. 3 (d, e and f), where the steep drop in stress after peak point should be attributed to fiber rupture (or loss of load bearing capacity if not ruptured). Therefore, it is reasonable to assume that adopting a constant fiber strength of 3000 MPa (highest reported value for steel fibers) does not have much influence in the accuracy of the proposed model, and the model should be directly applicable to the common range of fiber tensile strength of 2100~3000 MPa used in UHPFRC. Regarding the cases where fiber strength is lower than the value of 2100 MPa, a posterior modification can be performed in the proposed strength model. Particularly, the proportion of bridging stress contributed by ruptured fibers can be estimated (which is an easy task) and removed from the strength predicted by Eq. (13). The modified ultimate strain can be estimated as the strain corresponding to the modified strength in the original stress—strain model predicted by Eq. (27). Other parts of the stress—strain model should be maintained.

It should be noted that different specimen sizes may lead to different fiber orientations, and in turn different stress-strain behavior of UHPFRC (Frettlöhr et al. 2012). In the FEM simulations we adopted the same fiber orientation by referring to those observed by Yoo et al. (2014) and by Yu et al. (2022) with the specimen cross-section dimensions of 100×100 mm, and 50×50 mm, respectively. Both of them reported similar fiber orientations irrespective of the specimen cross-section dimension, fiber length or fiber content. The range of the specimen cross-section sizes reported in the experimental tests involved in the regression analysis is between 30×13 mm and 100×50 mm (see Table E.4). Considering that the proposed stress-strain model predicted both the ultimate stress and ultimate strain of these tests with a reasonable accuracy, it can be concluded that the proposed model can provide satisfactory predictions of the tensile stress-strain behavior for different specimen cross-section sizes. On the other hand, size effects for UHPFRC has indeed been observed by some researchers (Frettlöhr et al. 2012; Zani et al. 2017). Thus, it can be envisioned that with the incorporation of size effects, the accuracy and robustness of the proposed stress-strain model can be further improved, at the cost of a slightly higher complexity. However, a rational mechanistic evaluation of the size effects can only be achieved when corresponding mechanical test results and corresponding mesoscale fiber orientation distributions are provided in a systematic manner, so that reliable numerical modeling and parametric analysis can be conducted.

The second application of the proposed model is on mechanical analysis of UHPFRC. It can be directly used in the smeared cracking model (De Borst 1987; Maekawa et al. 2003) as the tension stiffening law, or used in the concrete damaged plasticity model (Lee and Fenves 1998) to provide the uniaxial tensile stress-strain relationship. To completely define the complex nonlinear behavior of UHPFRC in the context of smeared cracking model (Hu et al. 2023), apart from the tension stiffening law, a shear transfer law (Hu et al. 2022; Wu et al. 2019) and a compressive stress-strain model (Naeimi and Moustafa 2021; Zhang et al. 2023) specific for UHPFRC should also be supplemented. By contrast, a sufficient concrete damaged plasticity model for UHPFRC (Farzad et al. 2019; Shafieifar et al. 2017) does not require an explicit shear transfer model, but rather the uniaxial tensile and compressive stress-strain relationships and damage evolution laws under tension and compression (Krahl et al. 2018), respectively, need to be provided.

When using the proposed stress-strain model in mechanical analysis, the ascending branch up to the ultimate point can be directly used as inputs, while the softening part needs to be transferred to a stress-crack opening curve since this part represents a localization behavior, with all the incremental strain contributed by the opening of a single critical crack. Since we have adopted a gauge length of 76 mm in our simulations, the crack opening is calculated as:

$$\delta = 76(\varepsilon - \varepsilon_{pc}^{reg}) \quad (35).$$

An alternative approach to determine the softening part as a stress-crack opening curve is through single cracking analysis (Yang et al. 2008). However, the so-obtained curve should be properly adjusted such that the starting pointing corresponds to the peak stress under multiple cracking $\sigma_{\mathrm{pc}}^{reg}$.

7. Conclusions

A generalized tensile stress—strain model for UHPFRC has been developed, which is valid for different matrix compressive strengths, fiber lengths, fiber diameters and fiber contents. The model was validated by comparing the predictions with the experimental data of UHPFRC in the literature, in terms of the tensile strength, ultimate tensile strain and the stress—strain curves up to ultimate states. The key conclusions reached are summarized as follows:

(1) It is feasible to derive generalized stress—strain models for complex composite materials based on finite element models and limited experimental data towards rational design. The developed model has reasonable accuracy towards full range of the tensile stress—strain response of UHPFRC, giving a MAPE of 12% for composites strength, a MAPE of 25.3% for ultimate strain of UHPFRC with strain capacity exceeding 0.3%, and softening branches agreeing with experimentations from various groups, which renders it sufficient for design purpose. Potential improvements on the present model could be targeted on a thorough evaluation of available models on matrix cracking stress, and choosing the best of them to apply in the proposed stress—strain model, or developing a more accurate model for the mean matrix cracking strength of UHPFRC if available models are not good enough.

(2) To further improve the accuracy and robustness of the present model, the size effects on the tensile behavior of UHPFRC could be incorporated. The size effects of UHPFRC can be studied through both experimental tests and finite element analysis. Particular interests could be put on the influence of specimen size on the fiber orientation distribution (FOD),

which could be the origin to size effects at the material level. This aspect could be verified by the FEM model adopted here. Then, embedded with the FOD—specimen size relationship, the present tensile stress—strain model could be modified to incorporate the FOD and in turn the specimen size as a new variable, rendering it more robust in design and structural analysis.

(3) The lower mean matrix cracking strength leads to the lower ultimate strength of UHPFRC, because a lower matrix cracking strength means more cracks to form at the ultimate state, and higher tensile stress of fibers at the section to form the final crack. Accordingly, the remaining fiber stress at the final crack to be developed and amplified by the snubbing effect is smaller, although the fiber tensile stress purely contributed by the normal fiber—matrix friction is quite similar for different crack densities.

(4) The assumption that the snubbing effect only prevails where the crack is initiated is reasonable, considering that the FEM model predicted well extensive experimental stress—strain curves in different aspects. However, more advanced pullout tests remain to be designed and conducted to investigate how the pullout force changes in the middle of the pullout process when the fiber inclination angle is gradually changed. Alternatively, mesoscale finite element analysis can be used to investigate this problem, with the advantage of providing more detailed micro-stress distributions and load-transfer mechanisms.

(5) With the decrease of the mean matrix cracking strength, the ultimate strain of UHPFRC slightly increases, while the average crack width decreases significantly. The root cause to this is that when a new crack initiates between two old cracks, the interfacial stresses in the vicinity of the two old cracks further develops without visible increase in crack widths. Moreover, the new crack only needs to open to a smaller crack width to reach a similar level of stress of old cracks, which induced high initial interfacial stresses around the new

crack. The increase in the number of cracks and the decrease in the average crack width jointly contribute to a slight increase in the ultimate strain of UHPFRC.

Appendix A. Differences in single cracking and multiple cracking analysis

A schematic illustration of the typical stress profiles of fiber and matrix in the single crack region and interacted crack region is presented in Fig. A.1. Notable differences in both the matrix and fiber stress profiles can be identified between the two areas, indicating that neither the load transfer distance nor the crack width in multiple cracking process can be calculated based on single cracking analysis.

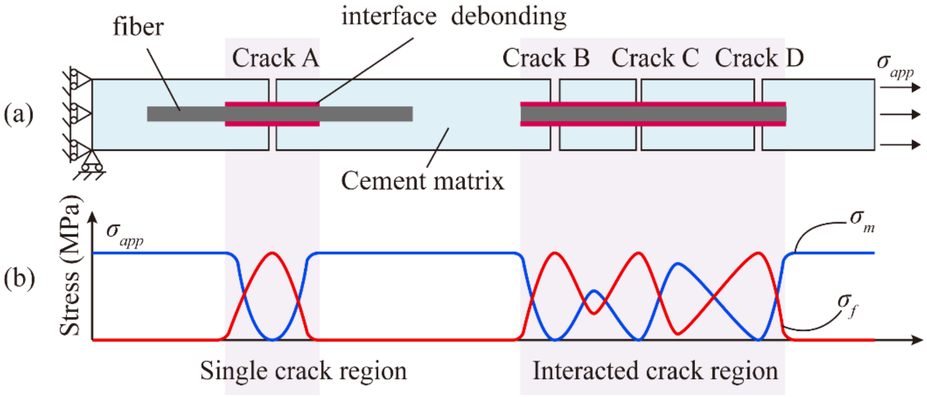

Fig. A.1. (a) A fiber bridging a single crack A and a fiber bridging three closely spaced cracks B, C and D in a composites specimen under uniaxial tensile stress σ_{app} ; (b) Profiles of the matrix stress σ_m and fiber stress σ_f in the tensile specimen, underlining the notable differences between the single crack region and interacted crack region.

Appendix B. Basic assumptions of FEM model

In the design of ECC, the fiber, matrix and fiber-matrix interface properties are carefully tailored to meet the two criteria (Li 2003; Li and Leung 1992): (i) the peak fiber bridging stress is higher than the matrix cracking strength; (ii) the matrix fracture toughness is no more than the maximum complementary energy of fiber bridging law (σ—δ), i.e., the steady-state cracking criterion. The steady-state cracking is defined as the growth of a defect into a flat crack (i.e., constant crack opening δ_{ss} along the crack length) cutting through the matrix (Yang and Li 2007). Since the fiber bridging stress has not reached the bridging strength at the steady-state crack opening δ_{ss}, further loads cause the specimen to develop new flat cracks rather than fail it. This multiple cracking process endows the cementitious composites with strain hardening property.

In this scenario, the complex three-dimensional multiple cracking process of UHPFRC could be reduced to a one-dimension problem, under the following assumptions:

(i) The further cracking behavior of a flat crack does not rely on the path by which it forms (either growing from a defect as in reality, or instantaneously formed and opening to δ_{ss} as in the 1-D model).

(ii) All flat cracks cut the specimen perpendicularly to the loading axis under uniform tensile stress in the specimen cross section.

(iii) The enhancement on the mean crack initiation stress and the strain hardening effect of UHPFRC, both brought by steel fibers, are two independent mechanisms. Particularly, the steel fibers retain the full bridging potential although they have enhanced the mean microcracking stress of UHPFRC, which is instead assigned to the mean matrix cracking strength.

The assumption (i) is valid considering that in the process of forming a flat crack, either growing from a defect as in reality or instantaneously formed, and expanding as in the 1-D model, the whole crack monotonically opens to the same crack width δ_{ss}. Therefore, the history variables and bridging forces at the crack surface, and stress fields in the vicinity of the crack, should be identical in both cases, which in turn lead to identical cracking characteristics in both cases under further loading. The assumption (ii) was justified by the available experiments conducted by different researchers (Huang et al. 2021; Pereira et al. 2012; Wille et al. 2012; Yu et al. 2020), where in most cases the cracks were found to be approximately perpendicularly to the loading axis. Besides, even in two-dimensional numerical simulations on the uniaxial tensile tests of ECC (Donnini et al. 2021; Lancioni and Alessi 2020; Le et al. 2019), the cracks tend to propagate perpendicularly to the loading axis.

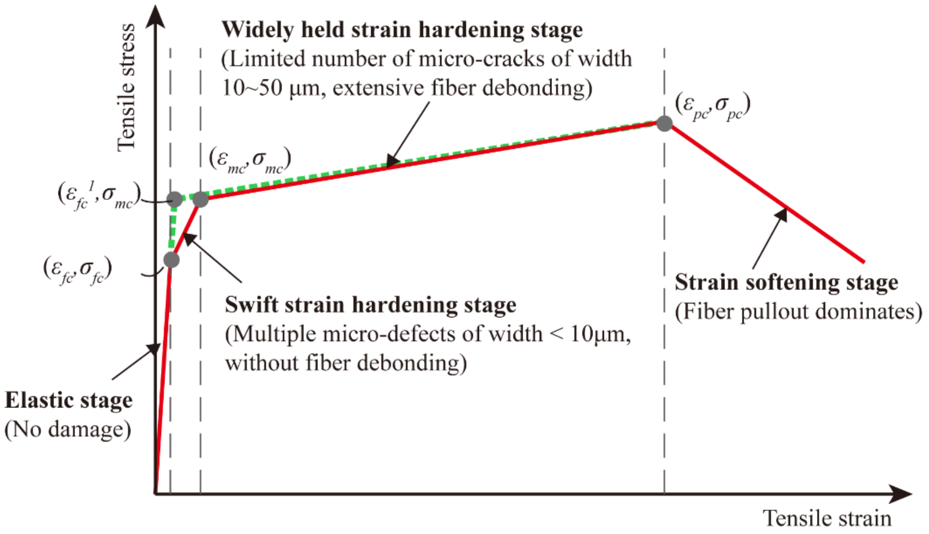

Fig. B.1. Typical tensile stress-strain curve of UHPFRC in the experiments, characterized by the three feature points: the first cracking point $(\varepsilon_{fc},\sigma_{fc})$, UHPFRC cracking point $(\varepsilon_{mc},\sigma_{mc})$ and the ultimate state point $(\varepsilon_{pc},\sigma_{pc})$, which divide the cracking process into four different stages: elastic stage, swift strain hardening stage, widely held strain hardening stage and strain softening stage (Bian et al. 2021). In the FEM simulations, the swift strain hardening stage is eliminated and the first two feature points collapse to the single UHPFRC crack initiation point $(\varepsilon_{fc}^{1},\sigma_{mc})$.

Regarding the assumption (iii), it was found that the strain hardening stage of UHPFRC could be further divided into two different stages: the swift strain-hardening stage with a higher deformation modulus, and the widely held strain hardening stage with a lower deformation modulus (Bian et al. 2021). Through acoustic emission, Bian et al. (2021) presented the strong evidences of multiple micro-defects (< 0.01mm) without fiber debonding at the swift strain hardening stage (Fig. B.1), while the widely held strain hardening stage is characterized by the formation of micro cracks with widths between 0.01 mm and 0.05 mm and extensive fiber debonding. The strongly different microscopic damage mechanisms and macroscopic deformation modulus manifested by the two different stages suggest that these two processes could be considered separately. Since currently the reinforcing mechanisms at the swift strain hardening process were poorly understood, the focus of the finite element analysis was on the widely held straining stage, and the stress at the end of the swift hardening stage was assigned to the mean matrix cracking stress (See σ_{mc} in Fig. B.1). This assumption was proved valid in subsequent sections. Indeed, the one-dimensional model concept has already been acknowledged by many researchers (Abrishambaf et al. 2019; Donnini et al. 2021; Huang and Zhang 2016; Lancioni and Alessi 2020; Li et al. 2019; Lu and Leung 2016; Shi and Leung 2017) when modeling the direct tension behavior of strain hardening cementitious composites.

Appendix C. Determining fiber orientation distribution and matrix strength distribution

Using a proper fiber orientation distribution (*FOD*) is crucial in accurately modeling the uniaxial tensile behavior of UHPFRC, including both the stress—strain behavior and cracking characteristics. Specifically, we referred to Yoo et al. (2014) who investigated the influence of fiber length on the *FOD*, and Yu et al. (2022) who studied the effect of fiber volume fraction on the *FOD* in UHPC. It was found that neither fiber length nor fiber volume fraction has a significant effect on the *FOD,* which suggested that it is feasible to adopt a unified *FOD* for differet UHPFRC. Moreover, the fibers were found to be oriented mainly between 22.5° and 45°. A further observation is that in both (Yoo et al. 2013; 2014) and (Yu et al. 2022), the probability density functions (PDFs) for *FOD* were all found to have two peaks: a larger peak at around 30° and a smaller peak at around 60°. These features for the *FOD* in UHPC was reproduced mathematically through the combination of two probability density functions $p_1(\theta)$ and $p_2(\theta)$, which have the following general form as proposed by Xia et al. (1995):

$$p(\theta) \frac{\sin(\theta)^{2r-1}\cos(\theta)^{2q-1}}{\int_0^{\frac{\pi}{2}}\sin(\theta)^{2r-1}\cos(\theta)^{2q-1}\mathrm{d}\theta}, \text{(C.1)}$$

with the two set of parameters $\left(r_1, q_1\right)$ and $\left(r_2, q_2\right)$ listed in Table E.1. Then, the unified PDF for the *FOD* of UHPFRC was defined as follows (see Fig. C.1 for a schematic illustration):

$$p^{comb}(\theta)=\begin{cases}\dfrac{p_1(\theta)}{\dfrac{\int_0^{50^\circ} p_1(\theta)\mathrm{d}\theta}{\int_0^{90^\circ} p_1(\theta)\mathrm{d}\theta}+\dfrac{\int_{50^\circ}^{90^\circ} p_2(\theta)\mathrm{d}\theta}{3\int_0^{90^\circ} p_2(\theta)\mathrm{d}\theta}}, \text{ if } \theta<50^\circ \\ \dfrac{p_2(\theta)/3}{\dfrac{\int_0^{50^\circ} p_1(\theta)\mathrm{d}\theta}{\int_0^{90^\circ} p_1(\theta)\mathrm{d}\theta}+\dfrac{\int_{50^\circ}^{90^\circ} p_2(\theta)\mathrm{d}\theta}{3\int_0^{90^\circ} p_2(\theta)\mathrm{d}\theta}}, \text{ if } \theta\geq 50^\circ\end{cases}. \quad \text{(C.2)}$$

It should also be noted that the matrix strength distribution along the loading axis was assumed to follow the Weibull distribution (Liu et al. 2022; Lu and Leung 2016) rather than being constant, in order to capture the sequential cracking feature as observed in the experiments. The Weibull distribution is characterized by two parameters: the scale parameter m and the shape parameter k. By adopting a sufficiently high value of k, the value of m would be approximately equal to the mean value of the quantity characterized. However, when k is too high, the matrix strengths for different potential cracks are indistinguishable, and rather smaller step sizes have to be adopted to ensure the crack is formed one by one, which limits the model efficiency. In the subsequent parametric analysis, the k value was set to be 100 for all cases, and thus the matrix crack strength was simply characterized by m, or the mean matrix cracking strength σ_{mc}. Alternatively, in the parameter identification process, a k value of 15 was adopted for all cases, to better characterize the grade in the cracking stresses before the widely held strain hardening stage, i.e. $\varepsilon_{app}=0 \sim 0.05\%$, as would be shown in the following results, while the m was selected by model fitting. Fig. C.2 illustrated the matrix strength distributions for $m=12\text{MPa}$ and two different k values of 15 and 100. It should be noted that due to the stochastic properties of the assumed matrix stength distribution as described in Seciton 3, the stress—strain curves from FEM simulations were not identical for different matrix strength distributions generated with the same Weibull parameters. Therefore, each data point was obtained by averaging the strengths and ultimate strains generaged by at least 5 FEM simulations to minimize the noise. An example of good convergence of the FEM model with respect to matrix strength randomness is illustrated in Fig. C.3. When convergence was not reached in 5 simulations, more simulations were conducted until a maximum of 10 simulations.

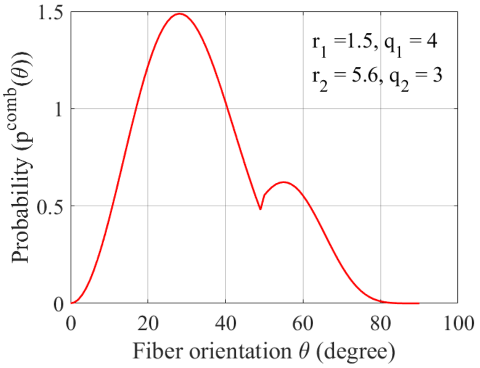

Fig. C.1. The probability density function $p^{comb}(\theta)$ for the steel fiber orientation distribution.

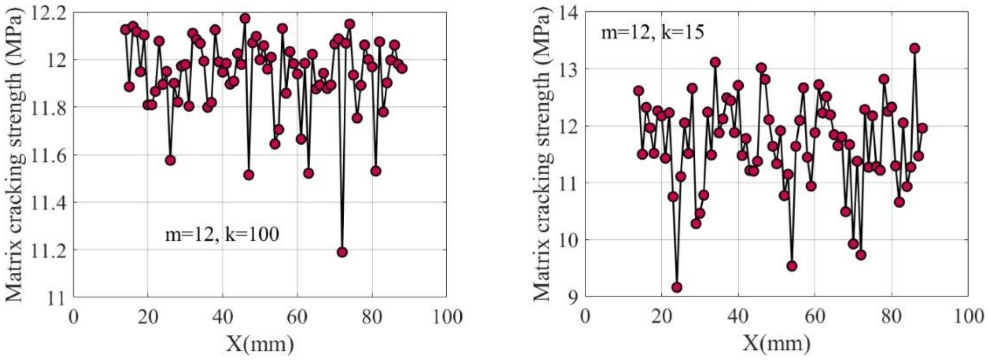

(a) (b)

Fig. C.2 Matrix strength distribution for the Weibull shape parameter k of (a) 100 and (b) 15.

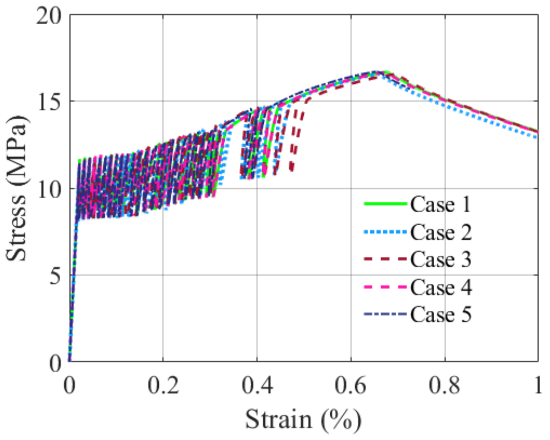

Fig. C.3 Five stress—strain curves simulated using five matrix strength distributions generated with the same Weibull parameters.

Appendix D. Ridge regression

Taking the derivation of the strength model of UHPFRC as an example (Section 4.1), Eq. (20) can be rewritten as：

$$\sigma_{pc}^{reg} = \sum_{i=1}^{4} b_i g_i = \begin{bmatrix} b_1 & b_2 & b_3 & b_4 \end{bmatrix} \begin{bmatrix} L_f^{\ e_1} D_f^{\ e_2} V_f^{\ e_3} \tau_0^{\ e_4} \\ L_f^{\ e_1} D_f^{\ e_2} V_f^{\ e_3} \tau_0^{\ e_4} \sigma_{mc}^{\ e_5} \\ L_f^{\ e_1} D_f^{\ e_2} V_f^{\ e_3} \tau_0^{\ e_4} k_i^{e_6} \\ L_f^{\ e_1} D_f^{\ e_2} V_f^{\ e_3} \tau_0^{\ e_4} \sigma_{mc}^{\ e_5} k_i^{e_6} \end{bmatrix}, \text{ (D.1)}$$

where g_i and b_i are the i th basis function and coefficient of σ_{pc}^{reg}, respectively. The ridge regression (Farebrother 1976) and trial and error analysis was employed to solve for the parameters $b_1 \sim b_4$ and $e_1 \sim e_6$, respectively. Specifically, different possible values of $e_1 \sim e_6$ were first assumed and substituted into Eq. (D.1), and the model parameters $b_1 \sim b_4$ was solved by minizing the L^2 - norm of the residual term:

$$b_i = \arg\min_{b_i} \sum_{j=1}^{N_{train}} \left(\left(\sigma_{pc}^{FEM} \right)^j - \sum_{i=1}^{4} b_i g_i^j \right)^2, \text{ (D.2)}$$

in which N_{train} is the total number of data points used to establish the regression model (Data 1~6 in Table E.3), $\left(\sigma_{pc}^{FEM} \right)^j$ is the composites strength predicted by the FEM simulation for data point j, and $f_i^{\ j}$ is the value of the i th basis at data point j. The ridge regression solves for $\mathbf{b} = \begin{bmatrix} b_1 & b & b_3 & b_4 \end{bmatrix}^T$ as follows:

$$\mathbf{b} = \left(\mathbf{G}^T \mathbf{G} + \lambda \mathbf{I}_4 \right)^{-1} \mathbf{G}^T \boldsymbol{\sigma}_{pc}^{FEM}, \text{ (D.3)}$$

where λ is the regularization parameter used to alleviate overfitting, with

$$\mathbf{G} = \begin{bmatrix} g_1^1 & g_2^1 & g_3^1 & g_4^1 \\ g_1^2 & g_2^2 & g_4^2 & g_4^2 \\ \vdots & \vdots & \vdots & \vdots \\ g_1^{N_{train}} & g_2^{N_{train}} & g_3^{N_{train}} & g_4^{N_{train}} \end{bmatrix}, \text{(D.4)}$$

$$\boldsymbol{\sigma}_{pc}^{FEM} = \left[\left(\sigma_{pc}^{FEM} \right)^1 \quad \left(\sigma_{pc}^{FEM} \right)^2 \quad \ldots \quad \left(\sigma_{pc}^{FEM} \right)^{N_{train}} \right]^T . \text{(D.5)}$$

Theoretically, various λ values are tried to solve for $\mathbf{b}$, and the derived regression model is examined by experimental data to find the λ which minimizes the mean absolute error :

$$\lambda = \arg\min_{\lambda} \frac{\sum_{j=1}^{N_{\exp}} \left| \left(\sigma_{pc}^{\exp} \right)^j - \left(\sigma_{pc}^{reg}(\lambda) \right)^j \right|}{N_{\exp}}, \text{(D.6)}$$

where $N_{\exp}$ is the number of experiment data and $\sigma_{pc}^{\exp}$ is the experimentally tested composite strength. The parameters $e_1 \sim e_6$ were determined in a brute force approach, i.e., looping all possible values of $e_1 \sim e_6$, performing the ridge regression following Eqs. (D.3~D.6), and finding the set of $e_1 \sim e_6$ which gives the lowest mean absolute error as expressed in Eq. (D.6).

Appendix E. Tables

Table E.1 Summary of the unified material parameters of UHPFRC.

Matrix	Steel Fiber	Interface
$E_m = 56$ GPa	$E_f = 210$ GPa	$\beta_f = -0.08$
$G_m = 0.02$ N/mm	$\sigma_f^y = 2600$ MPa	$w_{\mathrm{ref}} = 0.05$ mm
$k_{i_\Gamma}^0 = 1 \times 10^6$ MPa/mm	$r_1 = 1.5,\ q_1 = 4$	$f = 0.5$
$w^z = 5w^c$	$r_2 = 5.6,\ q_2 = 3$	$f' = 0.3$

Table E.2 Summary of the specific material parameters of UHPFRC for different cases.

	Fiber type	L_f (mm)	D_f (mm)	V_f (%)	τ_0 (MPa)	σ_{mc} (MPa)	k_i (MPa/mm)	f'_c (MPa)
Wille et al. 2014	S	13	0.2	2	12	11.8	4000	230
	S	13	0.2	2.5	12	12	4000	230
	S	13	0.2	3	12	12.5	4000	230
	T	18	0.3	1.5	16	8.7	4000	230

	T	18	0.3	2	16	10.9	4000	230
	T	18	0.3	3	16	13.3	4000	230
Wille et al. 2011	S	13	0.2	1.5	9	8	4000	190
	S	13	0.2	2	9	10.5	4000	190
	S	13	0.2	2.5	9	13	4000	190
	T	30	0.3	1	12	7.8	4000	190
	T	30	0.3	1.5	12	9.8	4000	190
	T	30	0.3	2	12	11.5	4000	190
Sujivorakul and Naaman 2003	T	30	0.3	1	8.5	3.5	1200	84
	T	30	0.3	1.5	9	3.5	1200	84
	T	30	0.3	2	9.5	3.5	1200	84
	T	30	0.3	4	9.5	3.5	1200	84
	T	18	0.3	2	9.5	7	1200	84
	T	24	0.3	2	9.5	5.5	1200	84
	T	30	0.3	2	2.3	3.1	150	20
	T	30	0.3	2	5	3.3	150	68

Table E.3 Parameters which were investigated in each data set.

	L_f (mm)	D_f (mm)	V_f (%)	τ_0 (MPa)	σ_{mc} (MPa)	k_i (MPa/mm)
Data 1	12, 13, 14, 15, 16, 17, 18	0.2	2	12	12	4000
Data 2	12	0.12, 0.13, 0.14, 0.15, 0.16, 0.17, 0.18, 0.19	2	12	12	4000
Data 3	12, 15, 18	0.12~0.3	1~3	8, 10, 12, 14	12	4000
Data 4	12, 15, 18	0.12~0.3	1~3	12	8, 10, 12, 14	4000
Data 5	12	0.12, 0.15, 0.2	2	8, 10, 12, 14	8, 10, 12, 14	4000
Data 6a	12, 15, 18	0.2	2	12	12	200, 400, 800, 1600, 3200
Data 6b	12	0.12, 0.15, 0.2	2	12	12	200, 400, 800, 1600, 3200
Data 6c	12	0.2	1.75~3	12	12	200, 400, 800, 1600, 3200
Data 6d	12	0.2	2	10, 12, 14	12	200, 400, 800, 1600, 3200
Data 6e	12	0.2	2	12	8, 10, 12	200, 400, 800, 1600, 3200
Data 7	13	$\frac{13}{60}, \frac{13}{80}, \frac{13}{100}$	1~2.75	12	8, 10, 12, 14	4000

Data 8	13	0.2	2, 2.5, 3	8, 10, 12, 14	8, 10, 12, 14	4000

Table E.4 Summary of the experimental data on UHPFRC tensile tests

Test No.	Data source	Fiber type	L_f (mm)	D_f (mm)	V_f (%)	f'_c (MPa)	σ_{mc} (MPa)	σ_{pc} (MPa)	ε_{pc} (%)	Specimen gauge length×width×thi-ckness
1	Wille et al. 2014	S	13	0.2	2	230	11.8	15	0.39	76×30×13 mm
2		S	13	0.2	2.5	230	12	16.5	0.47	
3		S	13	0.2	3	230	12.5	17.8	0.45	
4		T	18	0.3	1.5	230	8.7	11.1	0.38	
5		T	18	0.3	2	230	10.9	14.2	0.44	
6		T	18	0.3	3	230	13.3	19.6	0.41	
7	Wille et al. 2011a	S	13	0.2	1.5	190	8	8.3	0.17	76×30×13 mm
8		S	13	0.2	2	190	10.5	11.3	0.2	
9		S	13	0.2	2.5	190	13	14.2	0.24	
10		T	30	0.3	1	190	7.8	8	0.33	
11		T	30	0.3	1.5	190	9.8	11.6	0.47	
12		T	30	0.3	2	190	11.5	14.9	0.61	
13	Sujivorakul and Naaman 2003	T	30	0.3	1	84	3.5	5.94	1.01	75×25×25 mm
14		T	30	0.3	1.5	84	3.5	10.34	0.9	
15		T	30	0.3	2	84	3.5	13.39	1.29	
16		T	30	0.3	4	84	3.5	25.62	1.27	
17		T	18	0.3	2	84	7	8.44	0.37	
18		T	24	0.3	2	84	5.5	8.2	1.44	
19		T	30	0.3	2	20	3.1	3.69	0.43	
20		T	30	0.3	2	68	3.3	7.19	0.8	
21	Kim et al. 2012	T	30	0.3	1	28	2.64	3.2	0.35	177.8 × 50.8 × 25.4 mm
22		T	30	0.3	1	55	3	4.4	0.4	
23		T	30	0.3	1	84	4	5.5	0.62	
24		T	30	0.3	1	190	6	8	0.25	
25		T	30	0.3	2	28	3.67	5.14	0.33	
26		T	30	0.3	2	55	5.77	8.74	0.52	
27		T	30	0.3	2	84	7	10.8	0.45	

28		T	30	0.3	2	190	11	15	0.6	
29	Wille et al. 2011b	T	24	0.3	5.5	230	12	37.2	1.08	Not available
30		S	13	0.2	3	230	15	20	0.59	
31	Ryu et al. 2013	T	20	0.2	1	150	10.5	12.2	0.30	200 × 100 × 50 mm
32		T	20	0.2	1.5	150	11.1	14.3	0.82	
33		T	20	0.2	2	150	10.5	17.4	0.72	
34		T	22	0.22	1	150	10.5	13.3	0.3	
35		T	22	0.22	1.5	150	10.5	12.2	0.53	
36		T	22	0.22	2	150	12	15.3	0.64	
37		T	30	0.3	1	150	9.1	10.1	0.2	
38		T	30	0.3	1.5	150	10	11.1	0.65	
39		T	30	0.3	2	150	11	14.3	0.6	
40	Bian et al. 2021	S	16	0.2	2	190	10	13	0.5	200 × 100 × 50 mm
41		S	13	0.2	2	190	11	12	0.05	
42	Pyo et al. 2015	S	18	0.3	2	150	7.05	8.44	0.17	76×30×13 mm
43		S	25	0.2	1	150	6.22	7.5	0.33	
44		S	25	0.2	2	150	9.73	14.5	0.55	
45		S	25	0.4	2	150	6.86	8.32	0.27	
46		S	25	0.4	3	150	7.67	9.41	0.24	
47		T	25	0.3	1	150	6	7.5	0.19	
48		T	25	0.3	2	150	10	11.5	0.42	
49		T	25	0.3	3	150	11	20	0.48	
50		T	18	0.3	2	150	7.73	9.04	0.27	
51	Lao et al. 2022	S	13	0.2	3	163	11.5	16.6	0.5	76×30×13 mm
52		S	13	0.2	3	191	9	14.5	0.4	
53		S	13	0.2	3	200	9	12.5	0.35	
54		S	13	0.2	2	200	7.5	11	0.55	
55		S	13	0.2	4	200	12.5	18	0.35	

Table E.5 Specific parameters of interest in the parametric analysis

No.	L_f (mm)	D_f (mm)	V_f (%)	τ_0 (MPa)	σ_{mc} (MPa)	k_i (MPa/mm)

1	13	0.2	2	12	8	4000
2	13	0.2	2	12	10	4000
3	13	0.2	2	12	12	4000
4	13	0.2	2	12	14	4000

Declaration of Competing Interest

The authors declare that they have no known competing financial interests or personal relationships that could have appeared to influence the work reported in this paper.

CRediT authorship contribution statement

Wei-He Liu: Conceptualization, Methodology; Investigation, Validation, Visualization; Writing - Original Draft. **L.W. Zhang:** Methodology; Supervision; Review & Editing**. JG Dai:** Conceptualization, Funding Acquisition, Supervision, Writing - Review & Editing.

Acknowledgments

The authors acknowledge the supports provided by Chinese Guangdong Province R&D Plan for Key Areas (No. 2019B111107002), Hong Kong General Research Fund (RGC) (No. 15214517) and the Hong Kong Innovation and Technology Fund (No. ITS/077/18FX). Weihe Liu acknowledges the support by The Hong Kong Polytechnic University through the Research Institute for Land and Space (No. 1-CD7D).

References

Abrishambaf, A., Pimentel, M. and Nunes, S. 2019. A meso-mechanical model to simulate the tensile behaviour of ultra-high performance fibre-reinforced cementitious composites. Composite Structures 222, 110911.

Adeline, R. 1998. Design and behavior of the Sherbrooke footbridge, International Symposium of High Performance Concrete, Sherbrooke, pp. 89-98.

Aveston, J. 1971. Single and multiple fracture. The Properties of Fiber Composites, 15-26.

Aveston, J. and Kelly, A. 1973. Theory of multiple fracture of fibrous composites. Journal of Materials Science 8, 352-362.

Bache, H.H. 1981. Densified cement ultra-fine particle-based materials. In: Second International Conference On Superplasticizers in Concrete 10-12 June, 1981.

Bian, C., Wang, J.Y. and Guo, J.Y. 2021. Damage mechanism of ultra-high performance fibre reinforced concrete at different stages of direct tensile test based on acoustic emission analysis. Construction Building Materials 267, 120927.

Bitencourt, L.A., Manzoli, O.L., Bittencourt, T.N. and Vecchio, F. 2019. Numerical modeling of steel fiber reinforced concrete with a discrete and explicit representation of steel fibers. International Journal of Solids Structures 159, 171-190.

Carvalho, M.R., Barros, J.A., Zhang, Y. and Dias-da-Costa, D. 2020. A computational model for simulation of steel fibre reinforced concrete with explicit fibres and cracks. Computer Methods in Applied Mechanics Engineering 363, 112879.

De Borst, R. 1987. Smeared cracking, plasticity, creep, and thermal loading—A unified approach. Computer Methods in Applied Mechanics and Engineering 62, 89-110.

Donnini, J., Lancioni, G., Chiappini, G. and Corinaldesi, V. 2021. Uniaxial tensile behavior of ultra-high performance fiber-reinforced concrete (uhpfrc): Experiments and modeling. Composite Structures 258, 113433.

Farebrother, R.W. 1976. Further results on the mean square error of ridge regression. Journal of the Royal Statistical Society. Series B (Methodological) 38, 248-250.

Farzad, M., Shafieifar, M. and Azizinamini, A. 2019. Experimental and numerical study on bond strength between conventional concrete and Ultra High-Performance Concrete (UHPC). Engineering Structures 186, 297-305.

Fish, J., Wagner, G.J. and Keten, S. 2021. Mesoscopic and multiscale modelling in materials. Nature Materials 20, 774-786.

Frettlöhr, B., Reineck, K.-H. and Reinhardt, H.-W. 2012. Size and Shape Effect of UHPFRC Prisms Tested under Axial Tension and Bending. High Performance Fiber Reinforced Cement Composites 6: HPFRCC 6, 365-372.

Graybeal, B.J. 2011. FHWA TECHNOTE: Ultra High Performance Concrete. FHWA Publication No: FHWA-HRT-11-038: Federal Highway Administration.

Hu, X.-W., Ding, R., Zhang, Z.-Y. and Fan, J.-S. 2023. One-dimensional fiber beam-column model and two-dimensional fixed crack model for numerical simulation of UHPC structures. Engineering Structures 277, 115430.

Hu, Y., Qiu, J., Li, Z., Yao, Y., Liu, J. and Wang, J. 2022. Shear strength prediction method of the UHPC keyed dry joint considering the bridging effect of steel fibers. Engineering Structures 255, 113937.

Huang, B.-T., Zhu, J.-X., Weng, K.-F., Li, V.C. and Dai, J.-G. 2022. Ultra-high-strength engineered/strain-hardening cementitious composites (ECC/SHCC): Material design and effect of fiber hybridization. Cement and Concrete Composites 129, 104464.

Huang, B.T., Wu, J.Q., Yu, J., Dai, J.G., Leung, C.K.Y. and Li, V.C. 2021. Seawater sea-sand engineered/strain-hardening cementitious composites (ECC/SHCC): Assessment and modeling of crack characteristics. Cement and Concrete Research 140, 106292.

Huang, T. and Zhang, Y.X. 2016. Numerical modelling of mechanical behaviour of engineered cementitious composites under axial tension. Computers and Structures 173, 95-108.

Jiang, T. and Teng, J. 2007. Analysis-oriented stress–strain models for FRP–confined concrete. Engineering Structures 29, 2968-2986.

Kanda, T., Lin, Z. and Li, V.C. 2000. Tensile stress-strain modeling of pseudostrain hardening cementitious composites. Journal of Materials in Civil Engineering 12, 147-156.

Kim, D., Wille, K., Naaman, A. and El-Tawil, S. 2012. Strength dependent tensile behavior of strain hardening fiber reinforced concrete, High Performance Fiber Reinforced Cement Composites 6. Springer, pp. 3-10.

Krahl, P.A., Carrazedo, R. and El Debs, M.K. 2018. Mechanical damage evolution in UHPFRC: Experimental and numerical investigation. Engineering Structures 170, 63-77.

Krstulovic-Opara, N. and Malak, S. 1997. Micromechanical tensile behavior of slurry infiltrated continuous-fiber-mat reinforced concrete (SIMCON). Materials Journal 94, 373-384.

López, J.Á., Serna, P., Navarro-Gregori, J. and Coll, H. 2016. A simplified five-point inverse analysis method to determine the tensile properties of UHPFRC from unnotched four-point bending tests. Composites Part B: Engineering 91, 189-204.

Lancioni, G. and Alessi, R. 2020. Modeling micro-cracking and failure in short fiber-reinforced composites. Journal of the Mechanics and Physics of Solids 137, 103854.

Lao, J.C., Xu, L.Y., Huang, B.T., Dai, J.G. and Shah, S.P. 2022. Strain-hardening Ultra-High-Performance Geopolymer Concrete (UHPGC): Matrix design and effect of steel fibers. Composites Communications 30, 101081.

Larrard, F.d. and Sedran, T. 1994. Optimization of ultra-high-performance concrete by the use of a packing model. Cement Concrete Research 24, 997-1009.

Le, L.A., Nguyen, G.D., Bui, H.H., Sheikh, A.H. and Kotousov, A. 2019. Incorporation of micro-cracking and fibre bridging mechanisms in constitutive modelling of fibre reinforced concrete. Journal of the Mechanics and Physics of Solids 133, 103732.

Lee, J. and Fenves, G.L. 1998. Plastic-damage model for cyclic loading of concrete structures. Journal of Engineering Mechanics 124, 892-900.

Li, J., Weng, J. and Yang, E.-H. 2019. Stochastic model of tensile behavior of strain-hardening cementitious composites (SHCCs). Cement and Concrete Research 124, 105856.

Li, V.C. 2003. On engineered cementitious composites (ECC) a review of the material and its applications. Journal of Advanced Concrete Technology 1, 215-230.

Li, V.C. and Leung, C.K.Y. 1992. Steady- state and multiple cracking of short random fiber composites. Journal of Engineering Mechanics 118, 2246-2264.

Liu, W.H. and Zhang, L.W. 2019. A novel XFEM cohesive fracture framework for modeling nonlocal slip in randomly discrete fiber reinforced cementitious composites. Computer Methods in Applied Mechanics and Engineering 355, 1026-1061.

Liu, W.H., Zhang, L.W. and Liew, K.M. 2020. Modeling of crack bridging and failure in heterogeneous composite materials: A damage-plastic multiphase model. Journal of the Mechanics and Physics of Solids 143, 104072.

Liu, W.H., Zhang, L.W. and Liew, K.M. 2022. A cyclic plastic-damage multiphase model for evaluation of multiple cracking in strain hardening cementitious composites. Journal of the Mechanics Physics of Solids 158, 104692.

Lu, C. and Leung, C.K. 2016. A new model for the cracking process and tensile ductility of strain hardening cementitious composites (SHCC). Cement and Concrete Research 79, 353-365.

Lu, X., Teng, J., Ye, L. and Jiang, J. 2005. Bond–slip models for FRP sheets/plates bonded to concrete. Engineering Structures 27, 920-937.

Maekawa, K., Okamura, H. and Pimanmas, A. 2003. Non-linear mechanics of reinforced concrete. CRC Press.

Malak, S.A. and Krstulovic-Opara, N. 2019. Micromechanical Tensile Behavior of Slurry Infiltrated Mat Concrete with Inclined Fibers. ACI Materials Journal 116.

Massicotte, B. and Boucher-Proulx, G. 2010. Seismic retrofitting of bridge piers with UHPFRC jackets. Designing Building with UHPFRC: State of the Art Development, 531-540.

Mezquida-Alcaraz, E.J., Navarro-Gregori, J. and Serna-Ros, P. 2021. Direct procedure to characterize the tensile constitutive behavior of strain-softening and strain-hardening UHPFRC. Cement Concrete Composites 115, 103854.

Mi, R.J., Liew, K.M. and Pan, G.H. 2022. New insights into diffusion and reaction of CO2 gas in recycled aggregate concrete. Cement and Concrete Composites 129, 104486.

Mi, R.J. and Pan, G.H. 2022. Inhomogeneities of carbonation depth distributions in recycled aggregate concretes: A visualisation and quantification study. Construction and Building Materials 330, 127300.

Naaman, A.E. 2007. Tensile strain-hardening FRC composites: Historical evolution since the 1960, in: Grosse, C.U. (Ed.), Advances in Construction Materials. Springer Berlin Heidelberg, Berlin, Heidelberg, pp. 181-202.

Naaman, A.E. and Homrich, J.R. 1989. Tensile stress-strain properties of SIFCON. Materials Journal 86, 244-251.

Naaman, A.E., Namur, G., Najm, H. and Alwan, J. 1989. Bond mechanisms in fiber reinforced cement-based composites. Michigan Univ Ann Arbor Dep of Civil Engineering.

Naeimi, N. and Moustafa, M.A. 2021. Compressive behavior and stress–strain relationships of confined and unconfined UHPC. Construction and Building Materials 272, 121844.

Pereira, E.B., Fischer, G. and Barros, J.A.O. 2012. Direct assessment of tensile stress-crack opening behavior of Strain Hardening Cementitious Composites (SHCC). Cement and Concrete Research 42, 834-846.

Pyo, S., El-Tawil, S. and Naaman, A.E. 2016. Direct tensile behavior of ultra high performance fiber reinforced concrete (UHP-FRC) at high strain rates. Cement Concrete Research 88, 144-156.

Pyo, S., Wille, K., El-Tawil, S. and Naaman, A.E. 2015. Strain rate dependent properties of ultra high performance fiber reinforced concrete (UHP-FRC) under tension. Cement Concrete Composites 56, 15-24.

Qu, S., Zhang, Y., Zhu, Y., Huang, L., Qiu, M. and Shao, X. 2020. Prediction of tensile response of UHPC with aligned and ZnPh treated steel fibers based on a spatial stochastic process. Cement and Concrete Research 136, 106165.

Rebentrost, M. and Wight, G. 2009. Investigation of UHPFRC slabs under blast loads. Proceedings, Ultra-High Performance Fiber Reinforced Concrete 2009.

Ryu, G.S., Kim, S.H., Ahn, G.H. and Koh, K.T. 2013. Evaluation of the direct tensile behavioral characteristics of UHPC using twisted steel fibers, Advanced Materials Research, pp. 96-101.

Shafieifar, M., Farzad, M. and Azizinamini, A. 2017. Experimental and numerical study on mechanical properties of Ultra High Performance Concrete (UHPC). Construction and Building Materials 156, 402-411.

Shah, S.P. 1988. Theoretical models for predicting the performance of fiber reinforced concretes. Journal of Ferrocement 18, 263-284.

Shi, T. and Leung, C.K.Y. 2017. An effective discrete model for strain hardening cementitious composites: Model and concept. Computers and Structures 185, 27-46.

Stang, H. and Shah, S. 1986. Failure of fibre-reinforced composites by pull-out fracture. Journal of Materials Science 21, 953-957.

Sujivorakul, C. and Naaman, A. 2003. Tensile response of HPFRC composites using twisted polygonal steel fibers. Special Publication 216, 161-180.

Tan, W. and Martínez-Pañeda, E. 2021. Phase field predictions of microscopic fracture and R-curve behaviour of fibre-reinforced composites. Composites Science and Technology 202, 108539.

Tjiptobroto, P. 1991. Tensile strain hardening of high-performance fiber-reinforced cement-based composites. University of Michigan.

Tjiptobroto, P. and Hansen, W. 1991. Mechanism for tensile strain hardening in high performance cement-based fiber reinforced composites. Cement and Concrete Composites 13, 265-273.

Tjiptobroto, P. and Hansen, W. 1993a. Model for predicting the elastic strain of frc containing high volume fractions of discontinuous fibers. Materials Journal 90, 134-142.

Tjiptobroto, P. and Hansen, W. 1993b. Tensile strain hardening and multiple cracking in high-performance cement-based composites containing discontinuous fibers. Materials Journal 90, 16-25.

Vande Voort, T.L., Suleiman, M.T. and Sritharan, S. 2008. Design and performance verification of UHPC piles for deep foundations. Iowa State University. Center for Transportation Research and Education.

Wille, K., El-Tawil, S. and Naaman, A.E. 2014. Properties of strain hardening ultra high performance fiber reinforced concrete (UHP-FRC) under direct tensile loading. Cement Concrete Composites 48, 53-66.

Wille, K., Kim, D.J. and Naaman, A.E. 2011a. Strain-hardening UHP-FRC with low fiber contents. Materials and Structures 44, 583-598.

Wille, K., Naaman, A.E. and El-Tawil, S. 2011b. Optimizing ultra-high performance fiber-reinforced concrete. Concrete International 33, 35-41.

Wille, K., Naaman, A.E., El-Tawil, S. and Parra-Montesinos, G.J. 2012. Ultra-high performance concrete and fiber reinforced concrete: achieving strength and ductility without heat curing. Materials and Structures 45, 309-324.

Wu, P., Wu, C., Liu, Z. and Hao, H. 2019. Investigation of shear performance of UHPC by direct shear tests. Engineering Structures 183, 780-790.

Xia, M., Hamada, H. and Maekawa, Z. 1995. Flexural stiffness of injection molded glass fiber reinforced thermoplastics International Polymer Processing 10, 74-81.

Yang, E.H. and Li, V.C. 2007. Numerical study on steady-state cracking of composites. Composites Science and Technology 67, 151-156.

Yang, E.H., Wang, S.X., Yang, Y.Z. and Li, V.C. 2008. Fiber-bridging constitutive law of engineered cementitious composites. Journal of Advanced Concrete Technology 6, 181-193.

Yang, Y., Massicotte, B., Genikomsou, A.S., Pantazopoulou, S.J. and Palermo, D. 2021. Comparative investigation on tensile behaviour of UHPFRC. Materials and Structures 54, 1-19.

Yoo, D.Y., Kang, S.T., Lee, J.H. and Yoon, Y.S. 2013. Effect of shrinkage reducing admixture on tensile and flexural behaviors of UHPFRC considering fiber distribution characteristics. Cement and Concrete Research 54, 180-190.

Yoo, D.Y., Kang, S.T. and Yoon, Y.S. 2014. Effect of fiber length and placement method on flexural behavior, tension-softening curve, and fiber distribution characteristics of UHPFRC. Construction and Building Materials 64, 67-81.

Yu, J.J., Zhang, B.S., Chen, W.Z. and Liu, H. 2022. Multi-scale analysis on the tensile properties of UHPC considering fiber orientation. Composite Structures 280, 114835.

Yu, K.Q., Lu, Z.D., Dai, J.G. and Shah, S.P. 2020. Direct tensile properties and stress–Strain model of UHP-ECC. Journal of Materials in Civil Engineering 32, 04019344.

Zani, G., Colombo, M. and di Prisco, M. 2017. Size effect of HPFRCC in Tension. AFGC-ACI-fib-RILEM Int. Symposium on Ultra-High Performance Fibre-Reinforced Concrete, UHPFRC 2017 October 2-4, .

Zhang, H., Huang, Y.J., Yang, Z.J., Xu, S.L. and Chen, X.W. 2018. A discrete-continuum coupled finite element modelling approach for fibre reinforced concrete. Cement Concrete Research 106, 130-143.

Zhang, S.S., Teng, J.G. and Yu, T. 2013. Bond–slip model for CFRP strips near-surface mounted to concrete. Engineering Structures 56, 945-953.

Zhang, S.S., Wang, J.J., Lin, G., Yu, T. and Fernando, D. 2023. Stress-strain models for ultra-high performance concrete (UHPC) and ultra-high performance fiber-reinforced concrete (UHPFRC) under triaxial compression. Construction and Building Materials 370, 130658.

Zhang, X.F., Gao, J.L., O’Brien, D.J., Chen, W.N. and Ghosh, S. 2022. Parametrically-upscaled continuum damage mechanics (PUCDM) model for multiscale damage evolution in bending experiments of glass-epoxy composites. Composites Part B: Engineering 228, 109409.

Zhong, R., Zhang, F.L., Poh, L.H., Wang, S.S., Le, H.T.N. and Zhang, M.H. 2021. Assessing the effectiveness of UHPFRC, FRHSC and ECC against high velocity projectile impact. Cement and Concrete Composites 120, 104013.

Zhou, P.Z. and Feng, P. 2023. Unified analysis for tailorable multi-scale fiber reinforced cementitious composites in tension. Composites Part B: Engineering, 110586.

Zhu, Y.P., Zhang, Y., Hussein, H.H. and Qu, S.Q. 2021. Existing inverse analysis approaches for tensile stress–strain relationship of UHPC with treated steel fibers. Journal of Materials in Civil Engineering 33, 04021118.